

Earthquake source impacts on the generation and propagation of seismic infrasound to the upper atmosphere

Y. Nozuka,¹ P.A. Inchin,^{2,3} Y. Kaneko,¹ R. Sabatini^{2,4} and J.B. Snively²

¹*Department of Geophysics, Graduate School of Science, Kyoto University, Kyoto 606-8501, Japan. E-mail: nozuka.yoshito.75s@st.kyoto-u.ac.jp*

²*Department of Physical Sciences and Center for Space and Atmospheric Research, Embry-Riddle Aeronautical University, Daytona Beach, FL 32114-3900, USA*

³*Computational Physics, Inc., Springfield, Virginia 22151, USA*

⁴*Ecole Centrale de Lyon, CNRS, Université Claude Bernard Lyon 1, INSA Lyon, LMFA, UMR5509, 69130 Ecully, France*

Accepted 2024 May 9. Received 2024 May 8; in original form 2023 November 3

SUMMARY

Earthquakes with moment magnitude (M_w) ranging from 6.5 to 7.0 have been observed to generate sufficiently strong acoustic waves (AWs) in the upper atmosphere. These AWs are detectable in Global Navigation Satellite System satellite signals-based total electron content (TEC) observations in the ionosphere at altitudes ~ 250 – 300 km. However, the specific earthquake source parameters that influence the detectability and characteristics of AWs are not comprehensively understood. Here, we extend our approach of coupled earthquake-atmosphere dynamics modelling by combining dynamic rupture and seismic wave propagation simulations with 2-D and 3-D atmospheric numerical models, to investigate how the characteristics of earthquakes impact the generation and propagation of AWs. We developed a set of idealized dynamic rupture models varying faulting types and fault sizes, hypocentral depths and stress drops. We focus on earthquakes of M_w 6.0–6.5, which are considered the smallest detectable with TEC, and find that the resulting AWs undergo non-linear evolution and form acoustic shock N waves reaching thermosphere at ~ 90 – 140 km. The results reveal that the magnitude of the earthquakes is not the sole or primary factor determining the amplitudes of AWs in the upper atmosphere. Instead, various earthquake source characteristics, including the direction of rupture propagation, the polarity of seismic wave imprints on the surface, earthquake mechanism, stress drop and radiated energy, significantly influence the amplitudes and periods of AWs. The simulation results are also compared with observed TEC fluctuations from AWs generated by the 2023 M_w 6.2 Suzu (Japan) earthquake, finding preliminary agreement in terms of model-predicted signal periods and amplitudes. Understanding these nuanced relationships between earthquake source parameters and AW characteristics is essential for refining our ability to detect and interpret AW signals in the ionosphere.

Key words: Acoustic-gravity waves; Numerical modelling; Infrasound; Ionosphere/atmosphere interactions.

1 INTRODUCTION

Earthquakes act as impulsive sources of acoustic waves (AWs) generated in the atmosphere. These waves result from the transfer of momentum and energy at the interfaces between solids and air. AWs are mechanical waves with periods ranging from seconds to several hundreds of seconds that propagate in a gravity field (Press 1962). Due to the exponential decrease in atmospheric mass density with altitude, fluctuations of fluid velocity intensify as waves propagate upward to the upper atmosphere. As AWs travel through the thermosphere and ionosphere, typically at altitudes ranging from 100 to 500 km, they can induce density fluctuations in both neutral and

ionized constituents, which can be detected using modern remote sensing instruments.

One of the most common method for detecting seismically induced AWs is through the observation of total electron content (TEC). TEC relies on measuring the group delays and phase advances of Global Navigation Satellite Systems (GNSS) signals as they propagate through the ionospheric plasma, from satellites at $\sim 20\,000$ km to ground-based receivers (Calais & Minster 1998; Afraimovich *et al.* 2013). Unlike other observational techniques, which are often conducted within specific campaigns, GNSS signal measurements are continuous, networked and daily-updated datasets. Moreover, GNSS receivers offer extensive coverage in

seismically-active regions, receiving signals from multiple GNSS systems, including GPS, GLONASS, Galileo and Beidou. As a result, TEC observations have become a routine tool for investigating AW characteristics in the ionosphere (Komjathy *et al.* 2016).

Studies involving TEC observations of coseismic AWs help to understand earthquake source characteristics that contribute to the generation of AWs with sufficient amplitudes to be detectable (Sunil *et al.* 2021) and create opportunities to infer earthquake source parameters by examining the characteristics of GNSS TEC signals (Astafyeva & Shults 2019; Bagiya *et al.* 2023). Studies have investigated the link between earthquake magnitudes (M_w) and the amplitudes of TEC signals (Astafyeva *et al.* 2013; Cahyadi *et al.* 2015) and various indexes have been proposed to measure the relationship between TEC signal amplitudes and surface or ocean surface displacements (Manta *et al.* 2020). Results also suggest that earthquake source parameters such as focal depth, maximum vertical surface displacements (Sunil *et al.* 2021; Inchin *et al.* 2021) and direction of rupture propagation (Catherine *et al.* 2017; Inchin *et al.* 2020a; Meng *et al.* 2022) influence the amplitudes of AWs and the associated TEC signals. Understanding the vertical evolution of AWs and their observables in the upper atmosphere and ionosphere holds a potential for applications such as earthquake localization, characterization of earthquake sources, and determining the timing of wave generation (Afraimovich *et al.* 2006; Zedek *et al.* 2021). This knowledge may contribute to the development of warning systems, particularly for undersea earthquakes, that operate in near-real time (Inchin *et al.* 2020b; Maletckii & Astafyeva 2021; Brissaud & Astafyeva 2020; Martire *et al.* 2022). Such systems can provide information complementary to classical seismic, geodetic and ocean-based observations that may be limited in spatial and temporal resolution and coverage.

Studies that heavily rely on GNSS TEC observations of coseismic AWs may come with certain limitations. First, the observational geometries between ground-based receivers and GNSS satellites (i.e. line-of-sights, LOS) can be insufficient over the areas of interest, and may fail to capture important AW signals. Despite a large number of ground based receivers, TEC observations may still have limitations in terms of temporal and spatial coverage over near-epicentral regions and hinder a comprehensive understanding of the complex propagation of AWs. Complex plasma responses to AWs, as well as the presence of unrelated ionospheric dynamics, can further complicate the interpretation of TEC signals (Bravo *et al.* 2022). Even with sufficient coverage, investigations of AW propagation from the ground to the ionosphere and the dependence of wave parameters on earthquake source characteristics suffer from the inability to measure fluctuations at other altitudes other than ~ 200 – 400 km. While case studies supported by modelling efforts offer valuable insight into the evolution of AWs, their results may be limited in terms of generalization. Additionally, the detection of seismically excited AWs from earthquakes of magnitudes < 7 are still considered challenging (Sanchez *et al.* 2022). These events commonly represent the smallest earthquakes that can be reliably discerned using GNSS TEC (Perevalova *et al.* 2014). It remains unclear what specifically defines this threshold and whether earthquakes of similar or smaller magnitudes, which are more abundant compared to earthquakes with M_w 7–9, can be effectively targeted using TEC measurements or if alternative observational techniques can be explored.

In order to advance the understanding of coseismic AW generation and propagation to the upper atmosphere, we conducted a series of numerical modelling experiments to examine and expand upon previously drawn conclusions and findings from data-driven studies and case studies. To achieve this, we developed a set of

representative dynamic earthquake source models and performed 2-D and 3-D coupled solid-atmosphere simulations, spanning from the Earth's interior to the thermosphere. Through these simulations, we explored and investigated the key characteristics of earthquake sources that have previously been identified as playing a crucial role in the dynamics of AWs (Astafyeva & Heki 2009; Sunil *et al.* 2021; Meng *et al.* 2022). We focus on earthquakes with M_w 6.0–6.5, as they are reported to be close to the threshold of detectability with GNSS TEC (Perevalova *et al.* 2014). Additionally, we examined the evolution of AWs at lower altitudes (~ 80 – 200 km), where these waves could potentially be detected. We thus aim to improve the understanding of earthquake-related atmospheric processes to enhance the interpretation of observational data obtained through GNSS TEC measurements.

The paper is divided into the following sections. Section 2 provides the description of the modelling approach, assumptions and models and earthquake source configurations. Section 3 presents the results of simulations and their analysis. Discussion of the results is included into Section 4 and a summary of the study and future opportunities are provided in Section 5.

2 METHODS AND MODELLING APPROACH

We set up several earthquake source models of a thrust fault dipping 30° (Fig. 1a) and a pure strike-slip fault (Fig. 1b). To develop the earthquake models, we utilize dynamic rupture simulations, as opposed to a simpler, kinematic rupture approach, because dynamic rupture representation allows for a more realistic simulation of earthquake dynamics (Harris *et al.* 2018) and accounting for dynamic interactions of the propagating rupture and Earth's free surface is important for modelling realistic, near-field ground motions (Kaneko & Goto 2022). To limit the level of variability in the interpretation of the results, we assume planar rectangular fault in a 3-D, homogeneous elastic medium. Assigned wave speeds are 5.7 and 3.3 km s^{-1} for P and S waves, respectively. The magnitudes of normal and shear stresses increase linearly along dip, but are uniform along strike. Time-independent effective normal stress σ is assumed to follow:

$$\sigma = \rho g z (1 - \lambda) = 7.0z (\text{MPa}) \quad (1)$$

$$\tau = 0.55\sigma (\text{MPa}), \quad (2)$$

where g is gravity, z is the distance along dip (km), density $\rho = 2700$ kg m^{-3} and $\lambda = 0.74$ is the fluid pressure ratio (Harris *et al.* 2018). The friction acting on the fault is governed by the linear slip weakening law (Ida 1972; Palmer & Rice 1973), in which the frictional coefficient μ is determined as:

$$\mu = \mu_s + (\mu_d - \mu_s) \min(D/d_c, 1), \quad (3)$$

where μ_s and μ_d are static and dynamic frictional coefficients, respectively, D is a local fault slip and d_c is a characteristic distance. Rupture starts artificially within a small nucleation patch (dashed black circle in Figs 1a and b). Once the rupture nucleates, it propagates spontaneously outside the patch. The details of the nucleation procedure are described in the benchmark problem TPV22 (Harris *et al.* 2018). We perform dynamic rupture and seismic wave propagation simulations using SPEC3D (Komatitsch & Tromp 1999) with its numerical scheme based on the spectral element method (Ampuero 2002; Kaneko *et al.* 2008; Kaneko & Lapusta 2010), which has been verified through a series of community benchmark exercises (Harris *et al.* 2009, 2018). The simulations

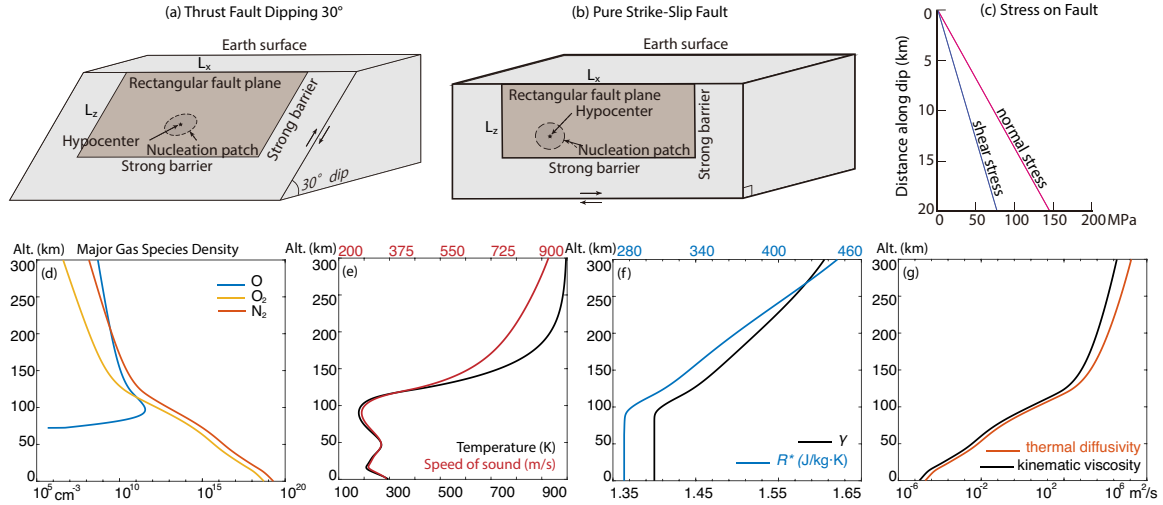


Figure 1. (a, b) Schematic representation of earthquake source geometry. (c) Diagram of normal and shear stresses at fault. Vertical profiles of (d) major atmospheric species densities, (e) temperature and speed of sound, (f) adiabatic index γ and specific gas constant R^* and (g) kinematic viscosity and thermal diffusivity.

resolve seismic waves for periods down to ~ 0.1 s, which is much smaller than the target period of ground velocities (~ 2 s and longer) that would matter for the generation of detectable coseismic AWs.

Vertical surface velocities, calculated in the seismic wave propagation simulations, are applied as bottom boundary condition of our 3-D numerical model MAGIC through momentum equation to simulate the generation and propagation of AWs, from surface to ~ 300 km altitude (Snively 2013; Inchin *et al.* 2020a, 2021). The bottom boundary of the MAGIC model, which is at the ground, is considered as rigid, taking into account large difference of solid and air densities. MAGIC solves the compressible, non-linear Navier–Stokes equations of the form:

$$\begin{cases} \frac{\partial \rho}{\partial t} + \nabla \cdot (\rho \mathbf{v}) = 0 \\ \frac{\partial \rho \mathbf{v}}{\partial t} + \nabla \cdot (\rho \mathbf{v} \mathbf{v} + P \mathbf{I}) = \rho \mathbf{g} + \nabla \cdot \boldsymbol{\tau} \\ \frac{\partial E}{\partial t} + \nabla \cdot ((\rho E + P) \mathbf{v}) = \rho \mathbf{g} \cdot \mathbf{v} + (\nabla \cdot \boldsymbol{\tau}) \cdot \mathbf{v} + k \nabla^2 T, \end{cases} \quad (4)$$

where ρ is density, \mathbf{v} velocity vector, P pressure, \mathbf{g} gravity, $E = \rho \epsilon + 0.5 \rho (\mathbf{v} \cdot \mathbf{v})$ total energy and $\epsilon = P/(\gamma - 1) \rho$ internal energy and γ adiabatic index, T temperature and $\boldsymbol{\tau} = \mu (\frac{\partial v_i}{\partial x_j} + \frac{\partial v_j}{\partial x_i} - \frac{2}{3} \delta_{ij} \frac{\partial v_k}{\partial x_k})$ - viscous stress tensor, k thermal conductivity and \mathbf{I} identity tensor. The details of MAGIC model formulation are provided in the appendix A of Zettergren & Snively (2015). Due to limited computational resources, it was unfeasible to perform all investigations within the 3-D atmospheric numerical model across all possible earthquake source parameter variations considered. Instead, we pursued a strategy involving 2-D atmospheric simulations as an initial exploration to identify the key earthquake source parameters influencing AW generation and propagation to the upper atmosphere. In the main text of this paper, we discuss the results of 3-D simulations, whereas the description of 2-D simulation approach and results are provided in the Appendix A to provide initial basis with associated caveats of their geometry. We note that while the model supports acoustic-gravity wave (AGW) modes of propagation, the periods observed in the simulations are decisively within the acoustic branch, for example ≤ 90 s, thus we refer to all as AWs.

Vertical profiles of temperature and major species densities (O, O₂ and N₂, which constitute >99 per cent of the atmospheric density) are derived from empirical model NRLMSISE00 (Picone *et al.* 2002) and are shown in Figs 1(d) and (e). From the composition

data the adiabatic index and specific gas constant are calculated, and thermal and momentum diffusivity are shown in Figs 1(f) and (j); these expressions are based on Heale *et al.* (2014) and references therein. To derive these profiles, we chose a location at $35^\circ\text{N}/120^\circ\text{E}$ and local time 12 p.m. on 28th of June, 2020. To simplify the analysis of the results, we do not include horizontal background winds into the simulations. We also do not vary profiles in horizontal direction and time, taking into account their negligible change over chosen numerical domains (~ 150 km \times 150 km) and time of wave propagation (~ 10 min). As only interested in AW propagation to the upper atmosphere, we developed and utilized an approach of moving vertically numerical domain framed only around AWs dynamics. To effectively use available computational resources and still capture the period of ground velocities at 2 s and longer, the initial resolution of MAGIC simulations is chosen as 100 m in horizontal and 40 or 50 m (for M_w 6.0 and 6.5 earthquake simulations, respectively) in vertical directions, and interpolated to a uniform 200 m as AWs reach altitudes of ~ 200 km and exhibit comparatively long periods, as well as longer wavelengths, due to the higher speed of sound.

3 RESULTS

This section is dedicated to analysing the outcomes of seismic wave and AW propagation simulations conducted under various scenarios of earthquake source scenarios. A summary of the earthquake sources is provided in Table 1. To obtain each source scenario, we varied the fault size, its depth, μ_d and μ_s , and conducted ~ 10 simulations to obtain desired M_w and stress drop. Stress drop of an earthquake is calculated via the spatial average of shear stress changes on the fault before and after the earthquake. The analysis begins by presenting simulation results for two M_w 6.5 earthquakes with different mechanisms: pure strike-slip and thrust (referred to as Sim #1 and #2). Subsequently, we discuss the simulation results for M_w 6.0 thrust earthquakes with two types of ruptures: unilateral and bilateral. These sources exhibit slightly different stress drops and depths of the faults (referred to as Sim #3 and #4). Finally, we present the results of three simulations involving M_w 6.5 earthquake sources with thrust mechanism and bilateral ruptures (referred to as Sim #5–7).

Table 1. Earthquake source parameters in simulations.

Sim #	Fault type/rupture type	Fault size ($L_x \times L_y$)/depth	$\mu_s/\mu_d/D_c$	Resulting M_w /stress drop
1.	Thrust/bilateral	20 × 10 km/0 km	0.75/0.45/0.3 m	6.5/4.3 MPa
2.	Strike-slip/unilateral	20 × 10 km/0 km	0.73/0.43/0.3 m	6.5/4.7 MPa
3.	Thrust/unilateral	12 × 6 km/1 km	0.72/0.42/0.15 m	6.0/5.6 MPa
4.	Thrust/bilateral	12 × 6 km/0 km	0.75/0.40/0.15 m	6.0/4.2 MPa
5.	Thrust/bilateral	29 × 14.5 km/0 km	0.55/0.53/0.3 m	6.5/1.2 MPa
6.	Thrust/bilateral	16 × 8 km/0 km	0.80/0.33/0.3 m	6.5/8.5 MPa
7.	Thrust/bilateral	19.5 × 9.5 km/10.1 km	0.61/0.51/0.3 m	6.5/8.4 MPa

We focus on the characteristics of AWs in terms of their vertical fluid velocities, which serve as a representative quantity for AW-driven fluctuations in the upper atmosphere. Fluid velocities are directly related to the momentum transfer between neutrals and ions/electrons, resulting in observable density fluctuations in the ionospheric plasma (Zettergren & Snively 2015). We acknowledge the cases where horizontal fluid velocity components can also play an important role, for example equatorial region, where magnetic inclination is practically zero; Mach number of acoustic fluctuations may also be a useful scalar diagnostic. In the discussion of AWs below, we strive to maintain a simplified perspective while acknowledging the potential influence of specific magnetic field geometries and ionospheric plasma interactions that can be investigated in subsequent studies.

To simplify the text, we also introduce variables U and U' to represent vertical displacements and velocities at the surface, respectively. We use variable W to denote vertical fluid velocity perturbations driven by AWs in the atmosphere. For the sake of clarity, we define the centre of the numerical domains as ($X = 0, Y = 0$), and designate the positive and negative directions from this centre as $X+$ and $Y+$ and $X-$ and $Y-$, respectively. In our figures, we use the variable Z to denote altitude in kilometres. In order to provide further support for the discussion of our results, we have included animations of seismic wave dynamics at the surface and AW propagation for each simulation in the [Supporting Information](#).

3.1 Dip-slip versus strike-slip faulting M_w 6.5 earthquakes with surface ruptures

We first examine the results of Sim #1 and #2 where AWs for different fault mechanisms (pure strike-slip versus 30° dip thrust) of the M_w 6.5 earthquakes are simulated. Both simulations have comparable stress drops of 4.3 and 4.7 MPa. Fig. 2 displays the results of seismic wave and AW propagation simulations with panels on the left depict results from Sim #1 and panels on the right from Sim #2. For both earthquake scenarios, the fault size is set to 10 km along the dip direction and 20 km along strike direction. The rupture is bilateral for the thrust earthquake and it is unilateral with a nucleation patch located 6 km away from the fault centre for the strike-slip earthquake (Figs 2a–d). In both cases, the rupture initiates at a depth of 8 km along the dip direction and propagates the surface (Figs 2e–h).

In thrust earthquake case (Sim #1), the dynamics of the rupture result in a slip of 1.8 m along the dip direction. In contrast, the strike-slip case (Sim #2) exhibits only 0.24 m of slip along the dip direction (Figs 2j and l). Conversely, the along-strike slip reaches only 0.45 m for the thrust earthquake, while it peaks at 1.7 m in the strike-slip case at the surface (Figs 2i and k). The values of U' are comparable between the simulations, with maximum absolute values of 0.58 and 0.52 m s^{-1} in Sim #1 and #2, respectively (Figs 2n

and p). However, the final U vary significantly between the simulations, amounting to 0.74 and 0.12 m for the thrust and strike-slip earthquakes, respectively (Figs 2r and w). In the case of the strike-slip earthquake, U' is concentrated along the $X+$ direction, which corresponds to the direction of rupture propagation (Figs 2o, p and w). For the thrust earthquake, the largest U and U' are simulated around the rupture area (especially near the arrest locations) and towards $Y+$ direction, extending from the fault depth to the surface (Figs 2m, n and r).

The surface responses to seismic waves exhibit spatial complexity, evolving for approximately 20 s before leaving the numerical domain. These surface responses generate compactly propagating upward AWs. Detailed animations can be found in the [Supporting Information](#). The general dynamics of AW propagation is as follows. The speed of propagation of AWs is influenced by the stratification of atmospheric neutral mass density and its composition. Molecular nitrogen and oxygen (O_2 and N_2) dominate below the thermosphere, while atomic oxygen (O) dominates in the thermosphere (Fig. 1d). This variation in composition leads to changes in the specific gas constant R (around 288) and the adiabatic index γ (1.4) below approximately 80 km, and these values increase to 442 and 1.6, respectively, in the thermosphere at 300 km (Fig. 1f). The growth of AW fluid fluctuations, propagating upward in an atmosphere with exponentially decreasing mass density due to gravity, is compensated by thermoviscous dissipative processes, which increase by orders of magnitude (Fig. 1j). The phase speed of AWs is markedly influenced by the altitudinal structure of temperature, which varies from 269 to 345 m s^{-1} between the ground and $Z \sim 100$ km, and then rapidly increases in the thermosphere, reaching values of 840 m s^{-1} at $Z = 300$ km. As it will be discussed in detail below, the vertical propagation of initially linear AWs (W is $< 1 \text{ m s}^{-1}$, 0.02–0.2 per cent of local Mach number below 50 km height, Fig. 2aa), follows by their steepening and evolving to acoustic shocks (Fig. 2bb), which then merge to form acoustic shock N waves (Figs 2cc and dd).

The maximum absolute W reached 114 m s^{-1} at $Z = 153$ km in Sim #1, and 65 m s^{-1} at $Z = 135$ km in Sim #2 (Figs 2q and v). The periods of the formed acoustic shock N wave in the thrust earthquake simulation are $\sim 42, 58$ and 79 s at $Z = 150, 200$ and 250 km, respectively. In the strike-slip simulation, the periods are $\sim 33, 42$ and 62 s at $Z = 150, 200$ and 250 km, making them ~ 25 per cent shorter compared to the thrust earthquake case. We expect that shorter period of formed N wave in Sim #2, in comparison with Sim #1, results from smaller amplitudes of AWs generated in the atmosphere (with comparable periods of AWs between two simulations at the ground) and thus lesser lengthening of shock N waves in the thermosphere. When the front shock of formed acoustic shock N wave reaches $Z = 150$ km, the dominant wavelength (λ_z) of the N wave is 21 km. The corresponding λ_z values at the moments when the front shock reaches $Z = 200$ km and 250 km are 37 and 55 km, respectively. The acoustic shock N wave in Sim #2 is fully formed

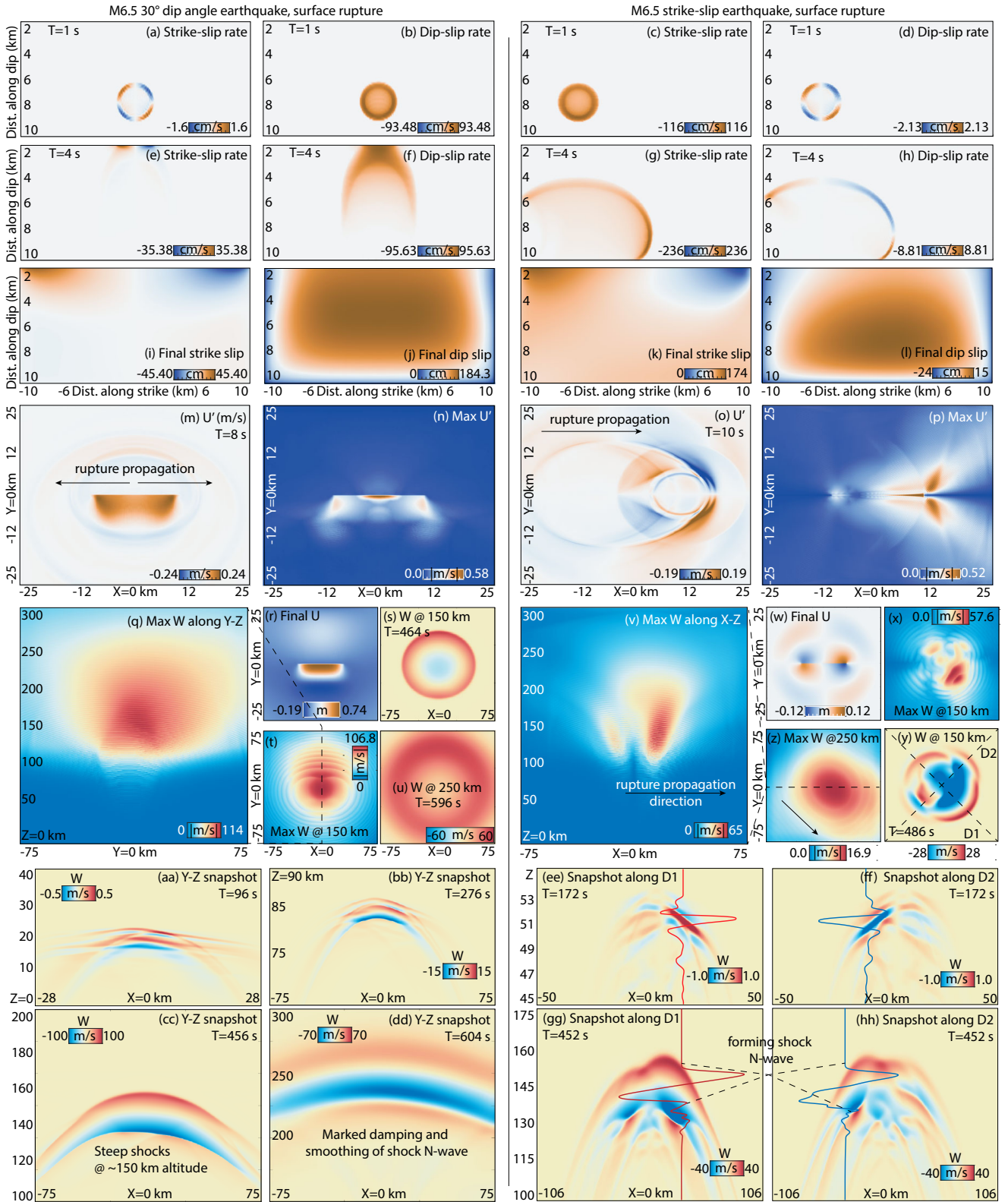


Figure 2. (a–h) The snapshots of strike- and dip-slip rates from Sim #1 (columns to the left) and Sim #2 (columns to the right) and (i–l) their respective final values. Panels (m)–(p), (r) and (w) illustrate the snapshots and maximum reached absolute velocity U' and final displacements U at the surface. Panels (s)–(u) and (x)–(z) illustrate the snapshots of W and maximum reached $|W|$ at $Z = 150$ and 250 km. (q, v) Maximum reached $|W|$ through the centre of the domain and along Y -axis for Sim #1 and X -axis for Sim #2. (aa–hh) The snapshots of W at different moments of time.

only when its front shock reaches $Z \sim 180$ km. The wavelength λ_z of the pulses are ~ 29 and ~ 43 km when the front shock is at $Z = 200$ and 250 km, respectively. The amplitudes of the AWs reach values of 62.64 and 34 m s^{-1} at altitudes corresponding to GNSS TEC observations ($Z = 250$ and 300 km) in Sim #1. In Sim #2, these corresponding amplitudes at the same altitudes are only 17 and 6.1 m s^{-1} .

Sim #2, which represents a strike-slip mechanism, exhibits significant horizontal asymmetry in W amplitudes in the upper atmosphere, towards the $X+$ direction and across Y -direction (Figs 2x–z and animation in the [Supporting Information](#)). This asymmetry is attributed to two main factors. First, it arises from the focusing of seismic waves and the subsequent generation of AWs in the atmosphere, towards the $X+$ direction, which corresponds to the direction of rupture propagation (Fig. 2p). Secondly, it is influenced by the different polarity of seismic wave imprints on the surface, occurring at $Y+$ and $Y-$ sides of the strike direction (Fig. 2o). Although the amplitudes of $|U'$ are similar in both directions from rupture at the surface (along Y -axis), the seismic waves induce dominant positive and negative polarized vertical responses on the surface (Figs 2o and p).

This asymmetry leads to the generation and initial propagation of AWs with fairly similar amplitudes but opposite polarities to $Y+$ and $Y-$ from rupture, as illustrated in snapshots of W along diagonals D1 and D2 (Figs 2ee and ff). These snapshots are retrieved from numerical domain diagonals as shown in Fig. 2(y) and are taken 172 s from the moment of rupture initiation (T_0) between 45 and 55 km altitudes. Here, the amplitudes of AWs of the dominant positive and negative pulses ± 8 km from the diagonals' centre have values of $W + 1.6$ and -1.59 m s^{-1} along D1 and D2, respectively. At altitudes between 100 and 175 km, the formation of acoustic shocks followed by their coalescence into acoustic shock N waves leads to the strongest fluctuations along diagonal D1, where dominant positive U are simulated (Figs 2o and gg). The maximum absolute amplitudes of W along positive and negative distances along D1 at $Z = 150$ km are 57 and 36 m s^{-1} , respectively. Along D2, the amplitudes of W towards positive and negative distances are 17 and 36 m s^{-1} , respectively. At higher altitudes ($Z > 200$ km), the strongest AWs still propagate towards the $X+/Y$ -direction, although this effect is less pronounced compared to lower altitudes due to the further extension of AW wavelengths resulting from the increase in the speed of sound and the elongation of formed acoustic shock N waves, which leads to superposition of waves (Fig. 1e). Lastly, the onset of AWs in the thermosphere towards $X+/Y-$ occurs earlier than in other directions within the numerical domain due to the larger amplitude of the formed front shock of the N wave towards $X+/Y-$ and its subsequent faster propagation compared to other directions. While the onset time difference is discernible at 150 km altitudes, it is less prominent at 250 km altitude.

Sim #1 also demonstrates some level of AW focusing towards $Y+$ direction, which is discernible even at thermospheric altitudes (Figs 2s–u). This difference in W along $X = 0$ slice at $Z = 150$ km and $Z = 250$ km at epochs $T_0 + 464$ s and $T_0 + 596$ s is 27 per cent ($38.3/52.5 \text{ m s}^{-1}$) and 19 per cent ($24.5/30.1 \text{ m s}^{-1}$), respectively.

3.2 M_w 6.0 earthquakes with dip-slip faulting

Here, we present the results of Sim #3 and Sim #4, which involve earthquake sources with M_w 6.0 (Table 1). The respective stress drops for these sources are 5.6 and 4.2 MPa. In Sim #3, the fault is slightly buried to a depth of 1 km, and the rupture is unilateral. In

Sim #4, the rupture reaches the surface and propagates bilaterally. Both sources have a fault size of 8×12 km along the dip and strike directions. In both cases, the rupture initiates at a depth of 4 km along the dip, but at 3 km away from the fault centre in Sim #3, and at the centre of the fault in Sim #4 (see the animation in the [Supporting Information](#)). The final slip along the dip direction is comparable between the simulations, with values of 96 and 86 cm for Sim #3 and Sim #4, respectively (Figs 3f and h). However, in Sim #4, where the rupture extends to the surface, larger slip along the strike direction is produced, reaching values of 11 cm, although localized near the rupture arrest locations (Fig. 3g). In contrast, Sim #3, with a buried fault of 1 km, exhibits only 1.4 cm of slip along the strike direction (Fig. 3e).

The snapshots of U' , as well as the maximum reached U and $|U'|$, are shown in Figs (i)–(l), (jj) and (ll). The final U in both simulations are comparable, measuring 0.36 in Sim #3 and 0.33 m in #4. The final maximum $|U'|$ are also similar on average (Figs 3j and l). However, the peak value of U' at the rupture arrest location in the $X+$ direction is 69 cm s^{-1} in Sim #3, while in Sim #4 with bilateral rupture, U' peak value is 47 cm s^{-1} at both locations of rupture arrest.

Figs 3(m) and (o) illustrate the maximum $|W|$ reached in Sim #3 and #4. These slices are selected along strike direction for the centre of the numerical domain (i.e. along X). Similar to the case of the strike-slip earthquake (Sim #2), the unilateral rupture in Sim #3 results in the focusing of AWs towards the direction of rupture motion towards $X+$ direction (Fig. 3 m). In contrast, the bilateral rupture in Sim #4 leads in a wavefield of fluctuations along the X -direction that appears more uniform (Fig. 3o). The maximum $|W|$ values in Sim #3 reach 74.6 m s^{-1} at $Z = 138$ km and 70 m s^{-1} at $Z = 141$ km. The W amplitudes are 27 and 10 m s^{-1} at $Z = 250$ and 300 km, respectively, in Sim #3, while they are commonly 5 – 25 per cent lower in Sim #4. Note that a uniform-like acoustic shock N wave is already formed at an altitude of approximately 90 km in both scenarios, which is much lower than in the case of the strike-slip earthquake discussed earlier (Sim #2).

Figs 3(q) and (s) displays the spatial signal from atmospheric simulations at 3 moments of time: 400 , 480 and 560 s after T_0 for the position $X = 0/Y = 0$. The periodograms of signals for the range of altitudes of 100 – 300 km for $X = 0/Y = 0$ are provided in panels (r) and (t). Due to the elongation of the N wave and its subsequent damping from thermoviscous dissipation, the periods become longer at higher altitudes, measuring 18 , 36 , 44 and 68 s at $Z = 100$, 150 , 200 and 250 km, respectively. The spatial signal at $T_0 + 400$ s exhibits an N -wave shape with a front and a tail shock of amplitudes ~ 46 and -55 m s^{-1} , respectively. Over time, the front shock of N wave undergoes noticeable smoothing due to dissipation, while the tail shock reaches values of around -72 m s^{-1} at $Z \approx 150$ km. The evolution of AWs, their periods and amplitudes in the thermosphere in Sim #4 are fairly similar to those found Sim #3 and are illustrated in Figs 3(s) and (t).

3.3 M_w 6.5 earthquakes with different stress drops and fault depth

In this section, we present the results of Sim #5, #6 and #7, complementing the discussion with results from Sim #1. These simulations involve similar earthquake sources of M_w 6.5 with a thrust mechanism and bilateral rupture, but they differ in terms of the resulting stress drops and fault depth (Table 1). Specifically, Sim #5 and Sim #6 have stress drops of 1.2 and 8.5 MPa, respectively, representing a

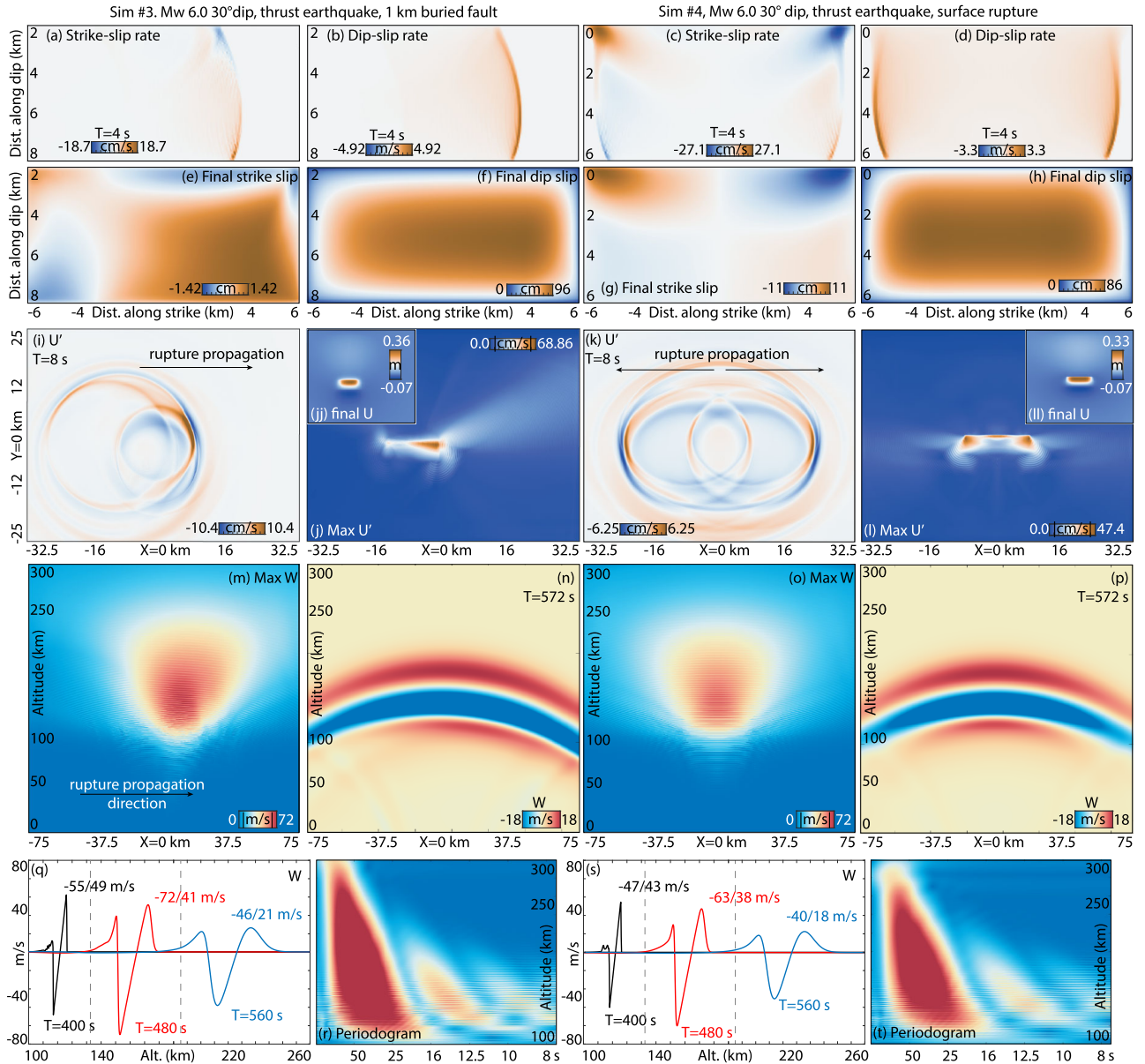


Figure 3. The results of Sim #3 and #4 from Table 1. (a–h) The results of seismic wave propagation on fault. Third row represent (i, k) the snapshots of U' , (jj, ll) final U and (j, l) maximum reached $|U'|$ at the surface. Bottom panels illustrate (n, p) W of AWs propagating in the thermosphere at $T = 572$ s and (m, o) maximum reached $|W|$. (q, w) Spatial signals of W along $X = 0/Y = 0$ in the thermosphere. (r, t) Periodograms of W with altitude along $X = 0, Y = 0$.

nearly sevenfold difference. To achieve this variation, the fault size specified as 29×14.5 km in Sim #5 and 16×8 km in Sim #6. Sim #7 has a similar earthquake source to Sim #6, with a fault size of 19.5×9.5 km and stress drop of 8.4 MPa, but the fault is buried to a depth of 10.1 km. Note that Sim #1 exhibits a comparable fault size (20×10 km) to Sim #7 but has a stress drop that is half the size, measuring 4.3 MPa. The maximum reached $|U'|$ vary significantly between the simulations, measuring 0.09, 0.58 and 0.23 m s^{-1} in Sim #5, Sim #1 and Sim #7, respectively. In Sim #6, the maximum value of $|U'|$ reaches 3.1 m/s . However, it is important to note that these are the maximum values observed very close to the rupture.

In all four scenarios, we observe a similar focusing of AWs towards $Y+$ direction, from the dip towards the surface of rupture (Figs 4e–h). Sim #5, which has the earthquake source with the

smallest stress drop of 1.2 MPa, exhibits the weakest AW amplitudes in the atmosphere, reaching peak value of $|W|$ only 88 m s^{-1} at $Z = 166$ km. Sim #1, with a stress drop of 4.3 MPa, demonstrates the second weakest AWs, with their peak $|W|$ of 114 m s^{-1} at $Z = 153$ km. Among the simulations with a ruptured surface, the strongest AWs are observed in Sim #6, which has a stress drop of 8.5 MPa. In this case, the AWs reach peak values of $|W|$ of 133 m s^{-1} at $Z = 145$ km. Interestingly, although to a comparatively small value, the strongest AWs are simulated in Sim #7, which has earthquake source similar to Sim #6, but includes a buried fault at a depth of 10 km. The AWs in Sim #7 reach their peak at the $Z = 179$ km and exhibit $|W| = 142 \text{ m s}^{-1}$. At the altitude of expected AW detections using GNSS TEC ($Z = 250$ km), the amplitudes of W reach values of 63, 48, 80 and 108 m s^{-1} and exhibit periods of 79, 72, 86 and 88 s in Sim #1, Sim #5, Sim #6 and Sim #7, respectively.

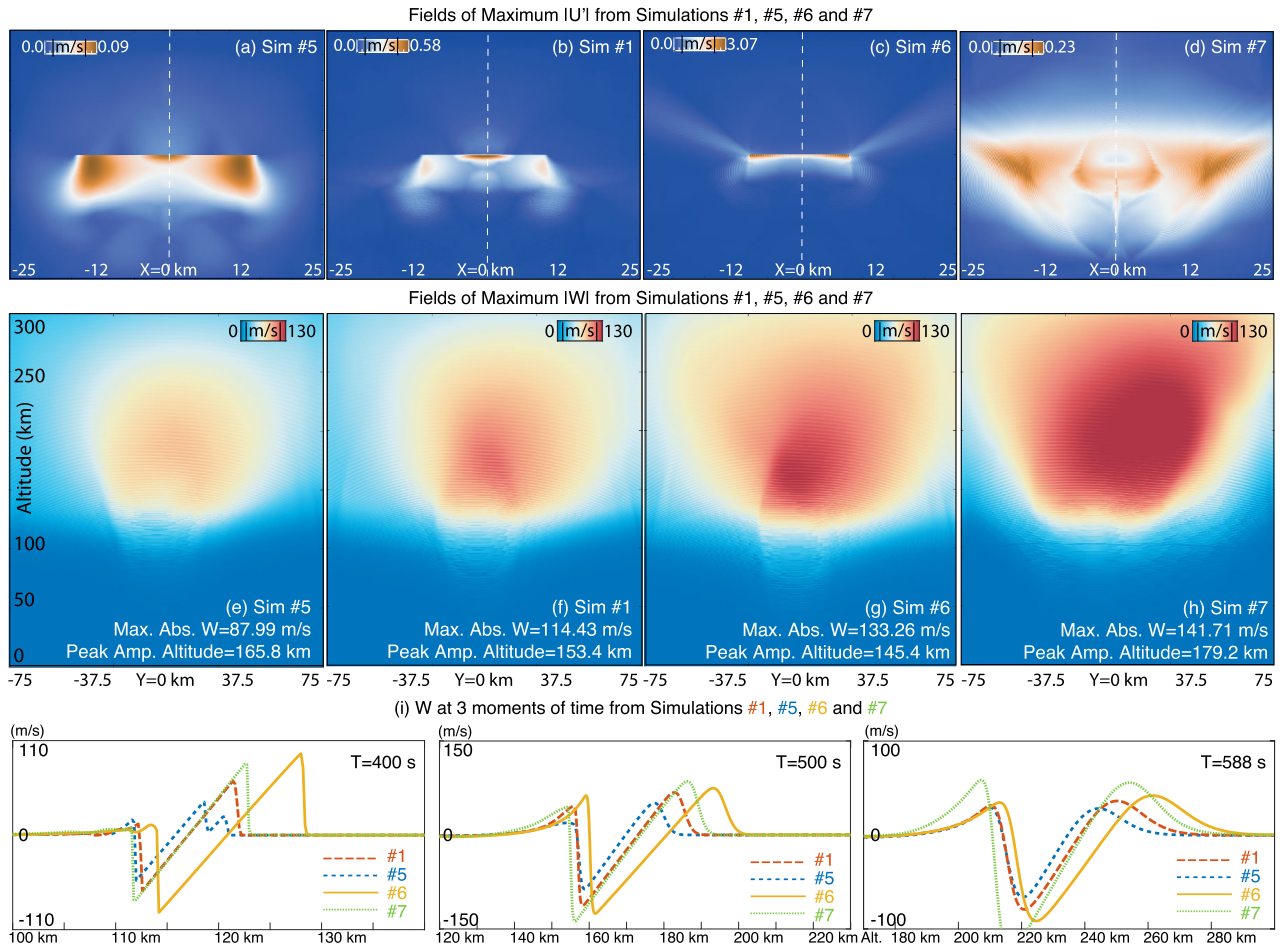


Figure 4. The results of Simulations #5, #1, #6 and #7 summarized in Table 1. (a–d) Maximum reached $|U'|$ at the surface, (e–h) maximum reached $|W|$ from the centre of the domain numerical and along Y -axis. Note that the results of Sim #5 are illustrated in most left-hand column. (i) Spatial signals of W during AW propagation in the thermosphere at 3 moments of time.

Table 2. Summary of simulation results.

Sim #	M_w /stress drop	Energy release (10^{13})	Max $ W $ and Z	Max W and T @ 250 km
1	6.5/4.3 MPa	10.5 J	114 m s^{-1} @ 153 km	62.6 m s^{-1} and 79 s
2	6.5 Strike slip/4.7 MPa	17.49 J	65.5 m s^{-1} @ 135 km	16.0 m s^{-1} and 62 s
3	6.0/5.6 MPa	3.18 J	74.6 m s^{-1} @ 138 km	26.6 m s^{-1} and 68 s
4	6.0/4.2 MPa	1.98 J	69.9 m s^{-1} @ 142 km	21.1 m s^{-1} and 66 s
5	6.5/1.2 MPa	4.59 J	87.9 m s^{-1} @ 165.8 km	47.9 m s^{-1} and 72 s
6	6.5/8.5 MPa	34.6 J	133 m s^{-1} @ 145 km	79.9 m s^{-1} and 86 s
7	6.5/8.4 MPa	28.9 J	141 m s^{-1} @ 179 km	108.0 m s^{-1} and 88 s

Fig. 4(i) displays the spatial signals over the centres of the domains ($X = 0/Y = 0$) at three different times from the simulations discussed in this section. The front shock of the formed acoustic shock N wave in Sim #6 propagates in the thermosphere ahead of front shocks in the other simulations (~ 5 – 20 km). This earlier propagation is due to the larger amplitudes of the formed shock N wave, which leads to greater lengthening of N wave (the values of maximum reach $|W|$, maximum $|W|$ and periods at $Z = 250$ km are provided in Table 2. The increased lengthening of the pulse also results in a longer period of the signal compared to Sim #1 and #5. On the other hand, the depth of the fault at 10 km in Sim #7 causes a slightly delayed arrival of the signal at

thermospheric heights, indicating that the fault depth affects the timing of signal arrival. Specifically, in Sim #7, the AW are generated seconds later than in case on a surface rupture. However, the front shock of N wave in Sim #7 still arrives earlier than the front shocks in Sim #1 and #5, highlighting the importance of the greater lengthening of N wave with stronger amplitudes of the front shock. The corresponding λ_z values when the front shocks of acoustic shock N waves reach $Z = 130$ km are 11, 13, 16 and 15 km in Sim #1, Sim #5, Sim #6 and Sim #7, respectively. Note that at this altitude, the AW waveform is not yet uniformly shaped to N wave in Sim #5 and individual shocks are still present (Fig. 4e).

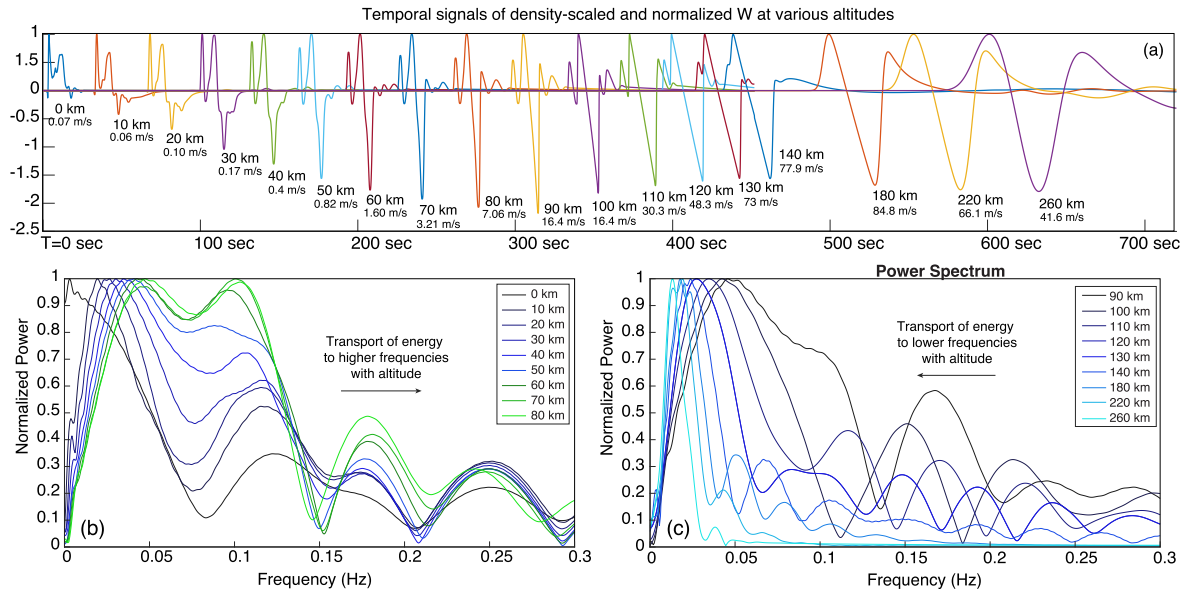


Figure 5. (a) Temporal signals of normalized density-scaled W at specific altitudes from Sim #5. For reference, the value of maximum absolute W is provided for each pulse. (b, c) Spectrograms of normalized power of signals illustrated in panel (a).

4 DISCUSSION

4.1 Non-linear evolution of coseismic AWs with altitude

First, we address the question raised by Astafyeva & Shults (2019)—*Can moderate earthquake generate shock waves?* by discussing the results of Sim #5, which are presented in Fig. 5. In Fig. 5(a), we illustrate the normalized density-scaled W at 18 different altitudes for the centre of the domain ($X=0/Y=0$). For reference, we provide the values of maximum reached $|W|$ for each altitude. The signals are depicted on one temporal axis at times of signal recordings. Figs 5(b) and (c) show the normalized power spectra of all the signals shown in panel (a). We expect that this M_w 6.5 earthquake can be considered as a moderate one, and the results and discussion below are applicable to earthquakes of comparable or larger magnitudes.

One observes linear AW signals in the lower atmosphere, as well as a linear-looking signal at altitudes where GNSS TEC detection occurs. Specifically, at $Z=260$ km the signal exhibits approximately 6 per cent of the local Mach number and less than 1 per cent at the ground. However, the dominant periods of these signals differ significantly, with seconds at the ground and approximately 72 s at $Z=250$ km. This discrepancy strongly suggests the non-linear evolution of the spectrum of AWs. The energy of the wave initially transitions to higher frequencies during their propagation up to $Z\sim 100$ km (Fig. 5b). However, the energy then transitions back to lower frequencies, with a sharp decrease in energy at frequencies above 0.05 Hz (Fig. 5c). This dynamic behavior is driven by the steepening of linear AWs into shocks, which subsequently merge to form an acoustic shock N wave at $Z\sim 140$ km. As the N wave continues to lengthen, its front and tail shocks are smoothed by thermoviscous dissipation, resulting in the sinusoidal-looking signal with a period of over a minute at altitudes above 200 km. The shapes of the signals depicted in Fig. 5(a) also illustrate such evolution.

The dynamics of AWs as described above are common in all the simulations we conducted and highlights the significant impact of non-linear effects on coseismic AWs, even for the smallest

earthquakes detectable with GNSS TEC. This evolution is primarily driven by the exponential decrease in atmospheric mass density with altitude and the conservation of wave energy, resulting in the growth of AW amplitudes (Hines 1960; Sabatini *et al.* 2016). Unlike explosions or explosive volcano eruptions that generate shocks at the source location, seismically generated AWs propagate in linear regime in the lower atmosphere and undergo a transition to non-linear regimes typically above the mesopause. This unique behavior of AWs generated by spatially extended earthquake ground motions has important implications for the analysis of coseismic AW signals in the upper atmosphere and ionosphere.

The non-linear evolution of AWs in the atmosphere may lead to the loss of information about the initial polarity of AWs. Previous data-guided studies have suggested the possibility of inferring surface uplift or subsidence based on the polarities of TEC signals (Astafyeva & Heki 2009; Chai & Jin 2021). However, our results show the formation of acoustic shock N waves in the lower thermosphere, which is much lower than the altitudes where GNSS TEC detections occur (around 250–350 km). As a result, the plasma density fluctuations observed in GNSS TEC are expected to reveal N waves with varying histories of damping and smoothing of their front and tail shocks due to thermoviscous dissipation. The observed initial decrease in electron density commonly found in GNSS TEC observations over the ruptured area should be attributed to the complex plasma drifts driven by AWs and the specific geometry of the observations rather than shape of AWs (Zettergren & Snively 2019; Inchin *et al.* 2021). Additionally, the polarity of surface vertical velocities caused by seismic waves does impact the characteristics of the resulting acoustic shock N waves in the upper atmosphere. The formation of individual shocks in initially differently shaped packets of AWs is followed by their different contributions during the merging process to form acoustic shock N waves. In the case of the pure strike-slip M_w 6.5 earthquake in Sim #2, the non-linear evolution of initially similar-shaped packets of AWs with reversed polarities results in a significant difference of ~ 40 per cent in the W amplitude of the formed N waves in the thermosphere. These

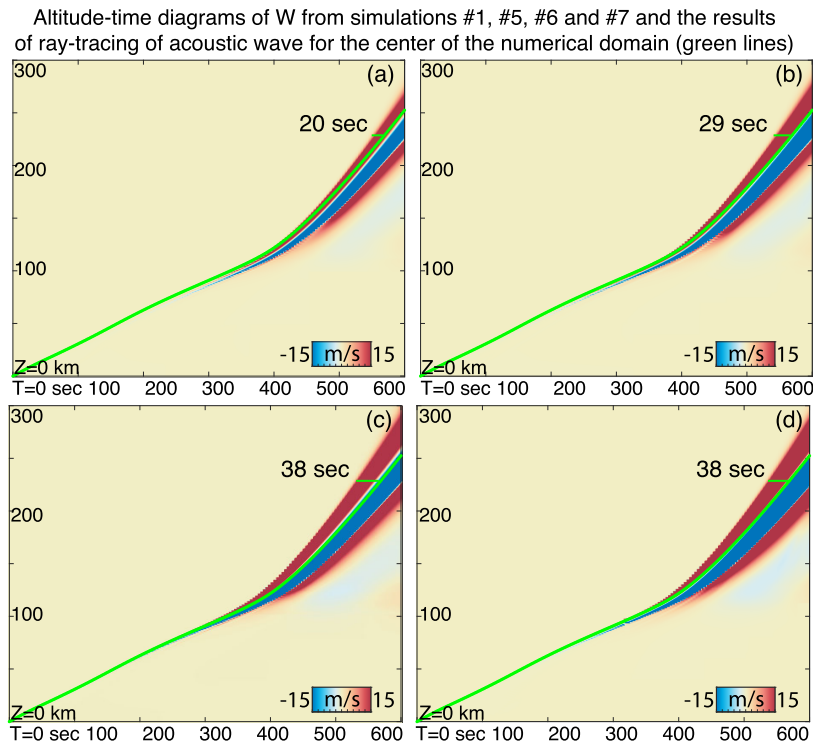


Figure 6. Time-altitude diagrams of W for the centre of the numerical domain from Simulations #1, #5, #6 and #7. Black line in each panel represents the results of ray tracing simulation of acoustic wave.

findings emphasize the complexity of AW dynamics and their modulation of plasma density in the upper atmosphere, highlighting the importance of considering the non-linear effects and the interaction between seismic waves and AWs and between AWs and ionospheric plasma motions in the interpretation of GNSS TEC signals.

The results also indicate that the arrival of N waves in the thermosphere can significantly differ from the arrivals calculated based on linear assumption of AW propagation based on local speed of sound (c_0) and thus the onset time of detected perturbation in GNSS TEC. Fig. 6 illustrates time-altitude diagrams of W for the centre of the numerical domain for Sim #1, #5, #6 and #7. In addition, we overlay the positions of rays of AW from ray tracing simulation. The atmospheric state for the ray tracing simulation is the same as for the MAGIC 3-D numerical simulations. The speed of sound is calculated as $c_0 = \sqrt{\gamma R^* T}$, where γ is the adiabatic index and R^* is the specific gas constant and T is the temperature. The initial direction of the ray demonstrated in the figure is specified to zenith and the integration in time is performed based on fourth-order Runge–Kutta algorithm. The position of rays are shown for the zero fluid velocity position, that is the bounding between positive or negative phase fronts.

While the onset time of zero fluid velocity point of the N wave at 250 km altitude is quite consistent between ray tracing and MAGIC simulations, Fig. 6 shows an earlier arrival of the leading shocks of N waves (at 20–38 s). This difference results from the variability of AW source, increase of AW wavelength in the thermosphere and non-linear expansion of acoustic shock N wave. The front shocks of N waves exceed c_0 and constitute a fraction of the local Mach number of 8.4–20 per cent at the altitude of 120 km. The dissipation of shocks leads to smaller fraction of Mach number at higher altitudes and constitutes 7.6–16.6 per cent at 150 km and 3.3–7.1 per cent at 250 km altitudes, respectively.

Therefore, while analysing GNSS TEC observations, the tracking of AW speeds based on the onset of fluctuations may lead to their markedly earlier arrivals, up to tens of seconds. This highlights the need to consider both the increase of AW wavelength due to the change of local speed of sound in the thermosphere and the lengthening of N -wave pulse when localizing AWs or AW sources (Zedek *et al.* 2021; Kakinami *et al.* 2021; Bravo *et al.* 2022). Note that for large magnitude earthquakes, when AW fluid velocities may constitute hundreds of m s^{-1} (Inchin *et al.* 2020a, 2021) in the thermosphere (i.e. be close to Mach number 1), the latter effect can be much more pronounced. The estimation of AW speeds based on tracking of the propagation of the centre point of the N wave (where the fluid velocity is zero) may be more suitable in this case. However, the shapes of GNSS TEC signals driven by AWs are influenced by the geometry of observation and the integration of electron densities along the line of sight (LOS). These signals may not necessarily resemble an N wave (to be used for the finding of centre point of N wave), exhibiting complex shapes and thus complicating the tracking of their propagation.

4.2 Earthquake source impacts

Our results reveal that the amplitudes of AWs in the upper atmosphere depend on various earthquake source characteristics, including the direction of rupture propagation, earthquake mechanism and stress drop, as summarized in Table 2. Below, we further analyse and elaborate on these results.

Previous research by Astafyeva *et al.* (2014) suggested that vertical surface displacements may not be the sole factor responsible for the excitation of strong AWs and thus ionospheric disturbances. Our simulations support this idea by demonstrating that earthquakes without significant surface uplift or subsidence, but with vertical

seismic wave projections to the surface, can still generate AWs that propagate to the upper atmosphere and potentially produce detectable signals (Tables 1 and 2; Figs S3c and S3d).

In addition, our simulations highlight the role of the source mechanism in the generation of AWs propagating upward. When comparing simulations with strike-slip and thrust earthquakes with the same magnitudes, stress drops and fault sizes, our models show significant differences in the amplitudes of the resulting AWs in the upper atmosphere. Specifically, the vertical fluid velocities driven by AWs peak at 65 and 114 m s⁻¹ for the strike-slip and thrust earthquakes, respectively. Moreover, the amplitudes of AWs generated by the M_w 6.5 strike-slip earthquake are even smaller than those generated by the M_w 6.0 thrust earthquakes at peaks or at altitude of GNSS TEC signal detections. These findings suggest that the detection of strong AWs in the upper atmosphere may provide valuable insights into earthquakes with tsunamigenic potentials, which are capable of causing large vertical ocean surface uplift and subsequent tsunamis (Kamogawa *et al.* 2016; Inchin *et al.* 2020b; Kanai *et al.* 2022).

The direction of rupture propagation plays a significant role in determining the spatial variability of atmospheric fluctuations generated by AWs, discernible even at thermospheric heights. This effect is not only observed for large magnitude earthquakes (Inchin *et al.* 2020a; Meng *et al.* 2022), but is also important for comparatively small magnitude earthquakes as considered here. Thus, we expect that the change of the direction of rupture propagation even on very localized faults, that is as in the case of the Papatea fault during the 2016 $M7.8$ Kaikoura earthquake, can still potentially be discerned with upper atmospheric and ionospheric observations (Inchin *et al.* 2021). Furthermore, the polarity of seismic wave imprints on the surface also has an influence on signals in the upper atmosphere due to the non-linear evolution of AWs with height. This implies that a comprehensive configuration of AW sources should be considered, as simply specifying a temporally varying offset would not lead to the excitation of realistic AWs. The non-linear behavior of AWs and their interaction with the atmosphere introduce complexities that should be taken into account when investigating the generation and propagation of AWs from earthquakes.

Our simulations reveal that the stress drop of an earthquake has a significant impact on the amplitudes of AWs in the upper atmosphere. Even with other parameters of the earthquake source being similar, earthquakes with different stress drops can lead to marked differences in the AW amplitudes (Figs 7a, b and S3a). Here, the amplitudes range from 87 m s⁻¹ at peak for a stress drop of 1.2 MPa to 133 m s⁻¹ for a stress drop of 8.4 MPa for M_w 6.5 thrust earthquakes. Despite the limited number of source scenarios we considered, AW amplitudes may be influenced by the stress drop of an earthquake. This conclusion is also supported by the results from simulations with M_w 6.0 thrust earthquakes, which show larger AW amplitudes for earthquakes with larger stress drops (Fig. 3). Since the stress drops of intraplate earthquakes are ~ 6 times larger than those of interplate counterparts (Scholz *et al.* 1986), these results suggest that the amplitudes of AWs from intraplate earthquakes would be generally larger than those from interplate events. This conclusion needs to be validated in future observational work.

The correlation between M_w 6.5 thrust earthquake stress drops and the amplitudes of AWs in the upper atmosphere motivates us to quantify the radiated energy of simulated earthquakes. The radiated energy E_r represents the seismic energy that would propagate to the far distance in a whole space with no attenuation. E_r of the earthquake model can be calculated via (Kostrov 1974; Kaneko &

Shearer 2014)

$$E_r = \int_{\Sigma} \frac{\tau^o(\xi) + \tau^f(\xi)}{2} S(\xi) d\Sigma - \int_0^{\infty} \int_{\Sigma} \tau(\xi, t) V(\xi, t) d\Sigma dt, \quad (5)$$

where τ is the shear stress on the fault, τ^o and τ^f are the initial and final shear stress, respectively, S and V are the slip and slip rate at a point on the fault ξ , respectively and Σ is the source area. Note that the calculation of radiated energy via eq. (5) is straightforward in a dynamic rupture model, but that is not the case in a kinematic source model, as it involves additional computation of shear traction changes from the fault slip histories. Since the characteristic slip d_c is assumed to be constant for a given M_w event (Table 1), larger stress drops generally mean larger radiated energy. Figs 7c,d illustrate the correlation between radiated energy at the fault and maximum amplitude of AWs and maximum amplitude of AWs at 250 km altitude from all simulations of this study. We find that, for a given fault type, radiated energy correlates well with AW amplitudes (see also and S3b). Strike-slip earthquake (Sim #2) produces weaker signals in the upper atmosphere compared to thrust earthquakes and are not expected to follow the inferred trend. Excluding strike-slip earthquake from the analysis yields Pearson's correlation coefficient r of 0.88 and 0.92 for maximum reached AWs and AW amplitudes reached at 250 km, respectively. These results make physical sense in that radiated energy of an earthquake is the total seismic energy flux over a spherical surface at a large distance around the source, which can be estimated via the time integral of the squared of velocity seismograms with a known focal mechanism (Haskell 1964; Rivera & Kanamori 2005) and that the input into the atmospheric model is the surface velocity albeit the vertical component only.

Our results do not indicate a significant impact of the size of the fault itself on the resulting AW amplitudes in the upper atmosphere. Simulations with larger fault sizes do not necessarily result in larger AW amplitudes, as seen in the comparison between a 29×14.5 km fault and a 16×8 km fault (both M_w 6.5 earthquakes). Similarly, the depth of the fault, at least for shallow earthquakes, does not appear to cause marked differences in the AW amplitudes in the upper atmosphere, although this may differ for deep (>70 km) earthquakes (Sunil *et al.* 2021). Conversely, the simulation with buried fault produced stronger fluctuations than the surface rupture counterpart with similar stress drop. This difference may be related to the difference in the frequency spectrum of surface ground velocities that lead to less dissipative acoustic shock N waves in the lower thermosphere, but future studies and simulations are required to clarify this point.

When acoustic shock N waves are formed in the lower thermosphere with longer periods, they are expected to penetrate into higher layers compared to N waves with shorter periods, assuming comparable other properties of AWs and atmospheric conditions. Without considering the non-linear evolution, the penetration of AWs is primarily controlled by their damping due to thermoviscous dissipation (Sutherland & Bass 2004). For M_w 7–9 earthquakes, the common periods of signals in GNSS TEC driven by coseismic AWs are ranging from ~ 3 to 8 min. In contrast, the periods of the signals simulated in our study do not exceed 1.5 min. The shorter period AWs simulated in our study do not exhibit large amplitudes (as for large earthquakes) penetrating to the bottom of the ionospheric F layer and the peak electron density altitude (approximately 250–350 km). Thus, the unfavorable detection of coseismic AWs from earthquakes with magnitudes of 6.0–6.5 or smaller can be attributed to the limited penetration of these AWs to higher altitudes and their

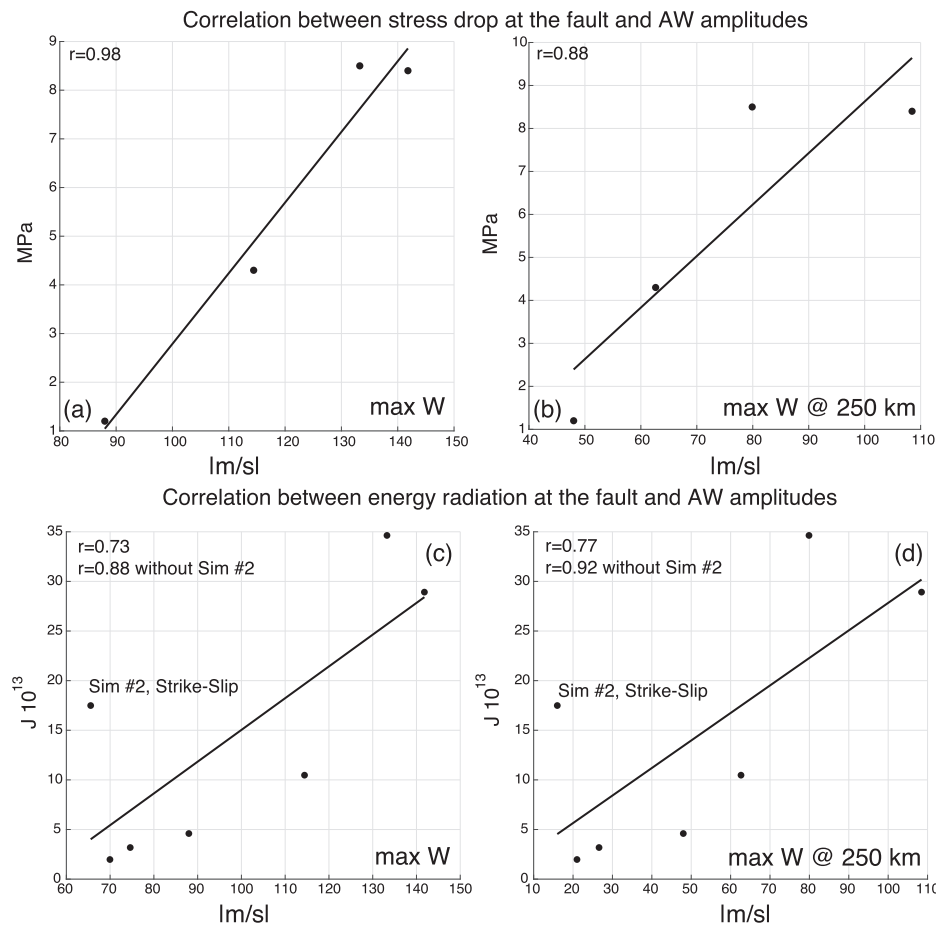


Figure 7. Correlations between maximum reached vertical fluid velocity (W) amplitudes of AWs and maximum reached W at 250 km altitude and (a, b) stress drop for M_w 6.5 thrust earthquake simulations and (c, d) radiated energy at the fault for all simulations of this study.

inability to generate detectable fluctuations in GNSS TEC measurements. Additionally, shorter period AWs have less ability to penetrate to higher altitudes as they are refracted by sharp temperature gradients in the thermosphere.

Our results indicate that the amplitudes of AWs in the thermosphere may not directly correlate with the M_w of an earthquake or the surface displacements caused by thrust earthquakes (Tables 1 and 2; Figs S3c and S3d), as suggested by previous studies (Astafyeva *et al.* 2013; Cahyadi *et al.* 2015; Manta *et al.* 2020). Instead, our findings suggest the need for a multiparameter analysis of earthquake sources and AW signals in the upper atmosphere to investigate their correlations. This analysis should consider various factors, including the mechanism of the earthquake, stress drop and radiated energy. Furthermore, our results reinforce that earthquakes cannot be treated as point sources of AWs, consistent with prior findings by, for example Inchin *et al.* (2021). The complexity of seismic wave imprints on the Earth's surface has a direct impact on the dynamics of AWs, even at distances hundreds of kilometres away from the source. This emphasizes the importance of considering the detailed seismic wave characteristics and their interactions with the atmosphere when studying AWs. Overall, our findings underscore the potential of utilizing upper atmospheric and ionospheric observations of coseismic AWs to gain insights into their earthquake sources. However, a comprehensive analysis taking into account multiple parameters is essential for accurately

inferring the characteristics of the seismic events based on AW observations.

The good correlation between radiated energy of an earthquake and the amplitude of AWs (Figs 7c and d) indicates that earthquake magnitude based on radiated energy (called energy magnitude, M_e , Choy & Boatwright 1995) may be a more important parameter controlling the excitation of AWs than moment magnitude. To test this idea, we analyse correlations between energy magnitude (M_e), moment magnitude (M_w) and the amplitudes of sTEC and vTEC for global large earthquakes (Fig. 8). We use estimates of M_e and M_w from Seismological Facility for the Advancement of Geoscience (IRIS) (IRIS DMC 2013), and compare the result for M_w previously reported in Cahyadi *et al.* (2015) and Astafyeva *et al.* (2014) (Fig. 8). M_e is calculated following $M_e = (2/3)\text{Log}_{10}E_r - 2.9$ (Choy & Boatwright 1995), where E_r is radiated energy at a broadband range (0.5–70 s) (IRIS DMC 2013). The correlation between M_e and the amplitudes of vTEC signals is comparable to the M_w counterpart. While it is difficult to assess if M_e or M_w correlates better with the amplitudes of vTEC due to overall linear relationship between M_w and M_e (Ide & Beroza 2001), the results from Figs 7 and 8 suggest that energy magnitude, which is a dynamic parameter, may be a more fundamental quantity controlling the excitation of AWs than moment magnitude, which is a static parameter. This idea is also consistent with the fact that even large ($M_w = 7$ or larger) slow slip events (slip episodes initiating in or near the seismogenic zone

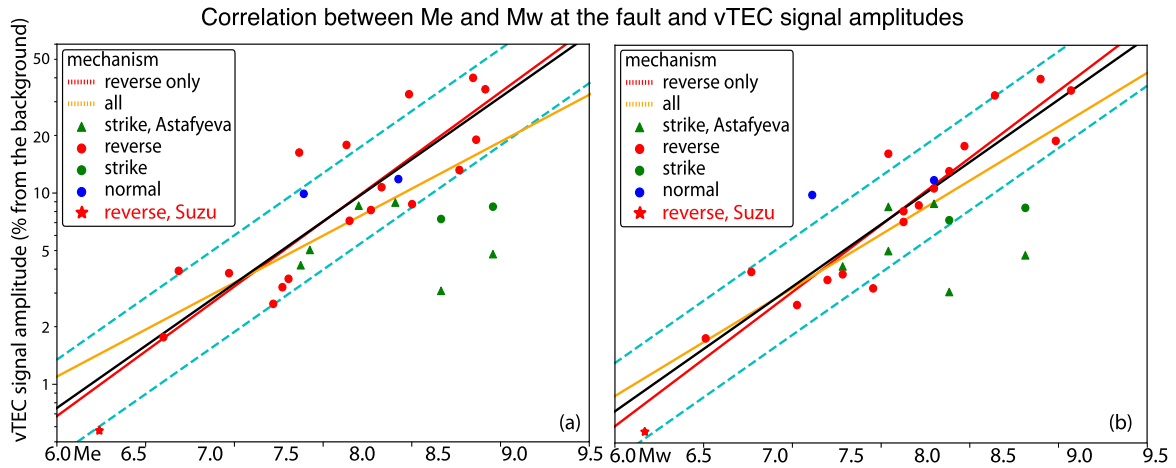


Figure 8. Correlations between energy magnitude (M_e), moment magnitude (M_w) and the amplitudes of GNSS vTEC signals as a per cent from the absolute vTEC. Circles filled with red, blue and green indicate the amplitudes of sTEC perturbations. The results are adapted from the Table A1 by Cahyadi *et al.* (2015) for reverse, normal and strike-slip respectively. Green triangles show the amplitudes of vTEC perturbations for strike-slip earthquakes discussed by Astafyeva *et al.* (2014). Black solid line indicates best-fitting line with the fixed slope of $2/3$ (Cahyadi *et al.* 2015). Blue dashed lines indicate uncertainties of factor two differences coming from non-ideal LOS geometry (Cahyadi *et al.* 2015). The red dashed line indicates the best-fitting line with both slope and offset inferred by linear regression for the 17 data of reverse earthquakes (Cahyadi *et al.* 2015). The yellow dashed line shows the best-fitting line inferred by linear regression for all the data plotted in this figure.

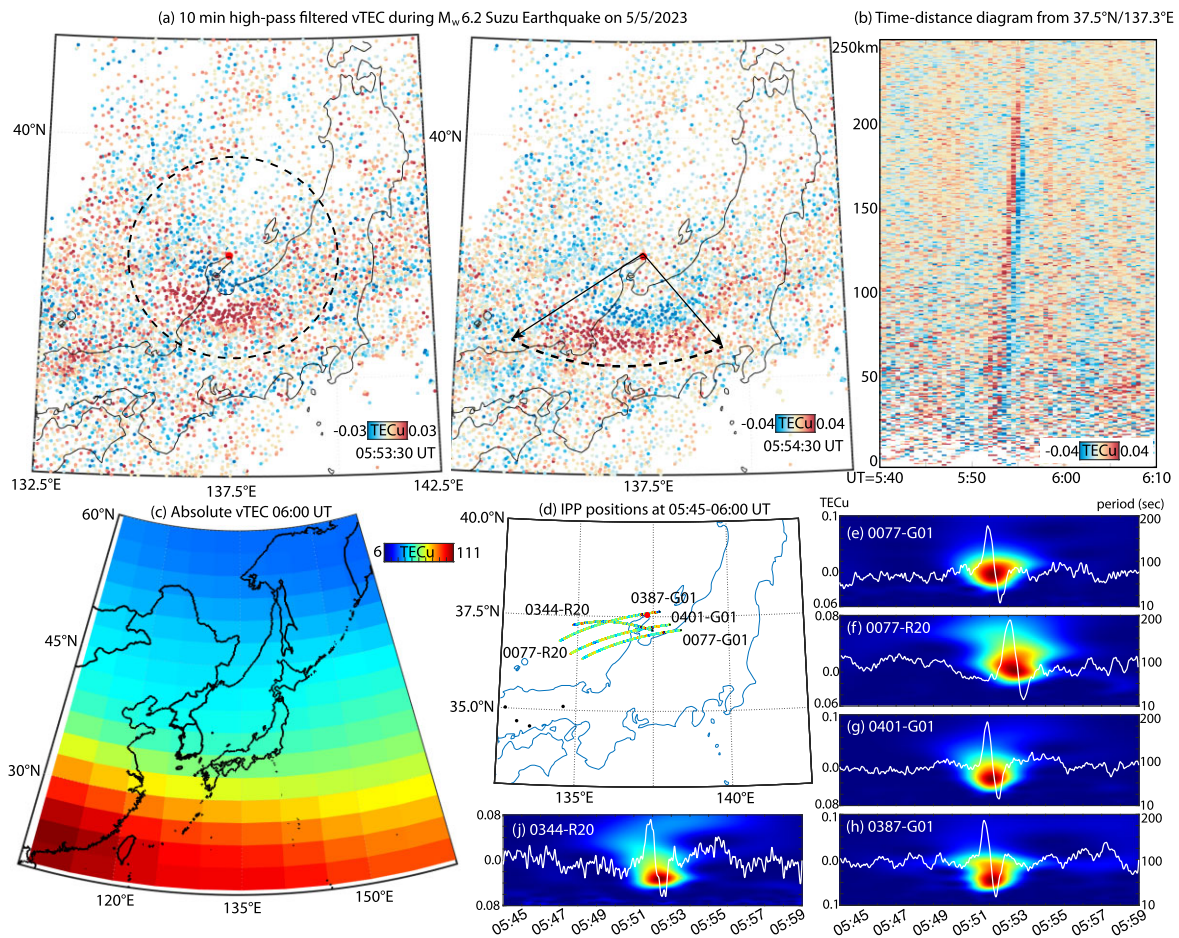


Figure 9. (a, b) The snapshots of vTEC observations processed with 10 min high-pass filter after the M_w 6.2 Suzu earthquake. (b) Time–distance diagram of 10 min high-pass filtered vTEC. The distance is calculated from the earthquake epicentre ($37.548^\circ\text{N}/137.299^\circ\text{E}$). (c) Absolute vTEC observations retrieved from Jet Propulsion Laboratory IONEX map. (d) Ionospheric pierce point (IPP) positions of vTEC observations processed with 10–600 s bandpass filter, which are demonstrated in panels (e)–(j).

and continuing for days to years but radiating no seismic energy, for example Schwartz & Rokosky 2007) do not excite detectable TEC perturbations in the ionosphere.

We caution that the reported TEC amplitudes in Fig. 8 may contain some biases due to several factors. First, the LOS geometries of TEC observations may not necessarily be aligned along the strongest fluctuations driven by AWs, as this particularly be true for near-epicentral region. The value of background vertical TEC (vTEC) is also limited by the use of specific algorithm for its estimation. From an AW dynamics perspective, the non-linear effects may lead to various evolution of waves to acoustic shock *N* wave, including the marked reduction of its amplitude via thermoviscous dissipation. Larger number of parametric simulations may help to clarify these biases in the future.

4.3 Coseismic AW detectability in the upper atmosphere and ionosphere

We acknowledge that the amplitudes of fluctuations observed in the atmosphere for the M_w 6.5 strike-slip and M_w 6.0 thrust earthquakes are comparable to those reported by Inchin *et al.* (2020a) for Rayleigh wave (RW) driven AWs. These amplitudes, on the order of tens of m s^{-1} in their fluid velocities, may result in TEC fluctuations at or slightly above the noise level of measurements (0.02–0.05 TECu). However, it is important to note that the specific conditions during the earthquake studied by Inchin *et al.* (2020a) (the occurrence at local noon and the presence of a equatorial ionospheric anomaly with high electron densities) may have favored the excitation of stronger plasma fluctuations. AW amplitudes at 250 km altitude for the thrust M_w 6.5 earthquakes range from ~ 50 to 110 m s^{-1} , which corresponds to around 18–40 per cent of the AW amplitudes we previously simulated and validated for the 2016 $M7.8$ Kaikoura earthquake in New Zealand (Inchin *et al.* 2021). Considering that TEC perturbations of approximately 0.2 TECu were observed for the Kaikoura earthquake, we anticipate that TEC perturbations driven by AWs with amplitudes of 50 – 110 m s^{-1} could potentially be detected under favorable conditions. Daytime ionosphere with high presence of electrons and line-of-sight (LOS) paths of GNSS TEC observations that cover lower altitudes and are parallel to the fronts of plasma fluctuations would be particularly favorable for these detections (Manta *et al.* 2020; Inchin *et al.* 2021).

Given that the periods of AWs simulated in our study range from approximately 1 to 1.5 min at an altitude of 250 km, it would be appropriate to utilize high-rate GNSS observations, such as those with a 1-s sampling interval, instead of the commonly used 15–30 s observations (which may be inappropriate for the investigation of short period signals). However, it is important to note that the period of the AW signals observed in GNSS TEC may not necessarily be the same as the period of the AWs themselves. This is due to next factors: (1) the plasma responses to AWs observed in TEC, which are aligned along magnetic field lines, (2) the integrated nature of TEC measurements and (3) the motion of the line-of-sight between the GNSS satellite and the receiver as it passes through plasma fluctuations. The latter introduces a Doppler shift effect, which can be particularly significant for observations made at low elevation angles (Inchin *et al.* 2020a). Finally, the spatial analysis of coseismic AW-driven TEC signals may be focused on the investigation of fluctuations with spatial characteristics of 40–80 km.

It is worth noting that the detection of AWs in E layer of the ionosphere (90–160 km) with GNSS TEC may be less likely, where AWs can exhibit comparatively large amplitudes even for earthquakes of

magnitudes 6.0–6.5 as demonstrated here. At these altitudes, the electron density is orders smaller than at the bottom of F layer, potentially precluding detections of fluctuations driven by AWs, which additionally may superimpose to ionospheric disturbances from higher altitudes. Future studies should be granted to understand the possibility to detect AWs in E layer of the ionosphere. At the same time, other observational techniques and instrumentation may be considered, which suit better AW detection in E layers of the ionosphere, for example ionosondes (Chum *et al.* 2012; Maruyama *et al.* 2017; Obenberger *et al.* 2022). The fluctuations driven by AWs in all considered here cases at mesospheric airglow altitudes (87–95 km) vary between 5 and 30 m s^{-1} of vertical fluid velocities and periods of 10–20 s (see animations in the Supporting Information). We expect that the detections of such small scale and short period signals may be limited to fortuitous cases.

4.3.1 The 2023 M_w 6.2 Suzu earthquake

To support the outcomes made based on numerical simulations reported in our study, we performed the analysis of GNSS TEC observations detected after the 5th of May 2023 Suzu earthquake. The magnitude of this reverse mechanism earthquake was estimated as 6.2 based United States Geological Survey (USGS). To calculate vertical TEC (vTEC), we used the algorithm and software discussed by Inchin *et al.* (2023). Raw GNSS observations in RINEX format were obtained from GNSS Earth Observation Network System (GEONET). Additionally, we used Jet Propulsion Laboratory (JPL) IONEX maps to estimate absolute vTEC over the region of interest. The earthquake occurred during local day time (14:42:04 LT, 05:42:04 UT) and the resulting AWs produced clearly detectable fluctuations in vTEC. Figs 9(a) and (b) illustrate the snapshots of 10 min high-pass filtered vTEC observations of 30 s sampling rate mapped with their respective ionospheric pierce point (IPP) positions onto the geographic map. The observations clearly indicate the fluctuations appearing ~ 10 min after the earthquake with their predominant direction of propagation equatorwardly. Fig. 9(b) demonstrates the time–distance diagram of observations to the south from epicentre location $37.548^\circ\text{N}/137.299^\circ\text{E}$. The fluctuations propagated from the epicentre position with speeds of around 0.9 – 1 km s^{-1} , indicating AWs as their sources, and are discernible for the distances of up to 250 km from the epicentre to the south.

Figs 9(e)–(j) demonstrate 1 sec sampling rate vTEC observations processed with 10–600 s bandpass filter and Morlet wavelet transforms are provided beneath each time series during 05:45–06:00 UT. The respective IPP positions for these observations are shown in Fig. 9(d). The estimated periods of pulses lie in the range of 63–74 s. The variability of pulse periods is likely driven by the motion of LOS, as well as integrated nature of TEC along LOS. These estimated periods of vTEC pulses support our numerical simulation results for the earthquakes of comparable magnitudes, which suggest periods in the range 62–88 s for thrust earthquakes. Also, the frontal and rear parts of the pulses are apparently steep, thus supporting our conclusion that AWs from even comparatively small amplitude earthquakes evolve to acoustic shock *N* waves. Finally, the maximum amplitudes of the pulses, estimated based on available observations, reached 0.09 TECu (Figs 9g and e). Having in mind that the absolute vTEC over the epicentral region is estimated as 41–44 TECu (see IONEX map at 06:00 UT in Fig. 9c), the fluctuations constitute 0.23 per cent from the background. This value is consistent with the estimations of correlations between M_w or M_e

and $v\text{TEC}$ signal amplitudes discussed above and shown in Fig. 8. The detectability of these signals would have been favored from day-time ionospheric state and thus comparatively high absolute $v\text{TEC}$.

5 CONCLUSION

In this study, we used dynamic earthquake source models to conduct comprehensive simulations investigating how different characteristics of earthquake sources influence the generation and propagation of AWs in the upper atmosphere. We specifically focused on earthquakes with M_w ranging from 6.0 to 6.5, which are typically considered close to the detectability threshold using Global Navigation Satellite System Total Electron Content (GNSS TEC) observations. Our simulations considered various earthquake source parameters, such as magnitude, earthquake mechanism, fault size, stress drop, radiated energy and rupture type. By constructing earthquake models that have different source parameters, we aimed to understand their specific effects on the resulting AW signals. The simulation results were supported by the analysis of coseismic AW signals in GNSS TEC observed after the 2023 M_w 6.2 Suzu earthquake. In doing so, we also sought to validate existing conclusions drawn from previous data-driven studies that investigated the relationship between earthquake sources and AW signals.

Our findings revealed that earthquakes in the M_w 6.0–6.5 range could generate AWs that undergo non-linear evolution and form acoustic shock N waves in the upper atmosphere. This non-linear evolution leads to the loss of information regarding the initial polarity of the AWs at the ground. We also found that the magnitude of the earthquakes is not the sole or primary factor determining the amplitude of coseismic AWs in the upper atmosphere. Instead, various earthquake source characteristics, including the direction of rupture propagation, the polarity of seismic wave imprints on the surface, earthquake mechanism, stress drop and radiated energy of an earthquake significantly influence the characteristics of the AW signals. In particular, our modelling results and data analysis suggest that energy magnitude of an earthquake may be a more fundamental parameter controlling the amplitude of TEC signals than moment magnitude.

Our study reinforces the understanding that earthquake source regions are not uniformly distributed nor can they be approximated as spherical in terms of their impact on the upper atmosphere and ionosphere. It highlights the value of conducting comprehensive analyses and quantifications of the parameters of acoustic shock N waves, including their amplitude, spectral content and onset times, with strong support from modelling. Although further efforts are needed to better constrain the complex chain of coupled processes involved and establish reliable links between them, our findings offer promise for leveraging upper atmospheric and ionospheric observations to infer information about seismic wave sources.

In future studies, it could be important to investigate the effects of topography on the radiation and propagation of AWs to the upper atmosphere. Although we focused solely on earthquake source impacts to simplify the analysis, considering topographic features can provide a more realistic representation of AW source geometry and, in vicinity to the surface, their propagation. Further investigations of additional earthquake source parameters, particularly those related to rupture propagation and surface dynamics, are needed to gain a more comprehensive understanding of AW generation and propagation. Performing such numerical simulations requires extensive computational resources, with our study requiring approximately

500 000 core-hours. This limitation restricts the number of simulations that can be conducted. While analytical or semi-analytical methods based on linear propagation theory, such as the one developed by Gao *et al.* (2023), could be used for efficient simulations of AWs, accounting for non-linear effects would be important in modelling realistic AWs in the upper atmosphere (Inchin *et al.* 2020a). Future advancements in numerical schemes and modelling techniques, such as adaptive mesh refinement, will help to increase the number of feasible simulations and allow for the construction of a comprehensive database for detailed analysis of the correlations between earthquake source characteristics and AW properties in the atmosphere.

ACKNOWLEDGMENTS

Research at the Earthquake Research Institute at the University of Tokyo was supported by JSPS KAKENHI (21H05206) and ERI JURP 2023-S-A102. Research at ERAU was supported by NASA Earth Sciences (ESI) 80NSSC22K0507 and DARPA Cooperative Agreement HR00112120003. This work is approved for public release; distribution is unlimited. The content of the information does not necessarily reflect the position or the policy of the Government, and no official endorsement should be inferred.

SUPPORTING INFORMATION

The datasets and animations of atmospheric simulation results, as well as necessary scripts, are provided through Embry-Riddle Aeronautical University Scholarly Data Commons: <https://datacommons.erau.edu/datasets/zyjxgxhgyt/1> (doi: 10.17632/zyjxgxhgyt.1).

Please note: Oxford University Press is not responsible for the content or functionality of any supporting materials supplied by the authors. Any queries (other than missing material) should be directed to the corresponding author for the paper.

DATA AVAILABILITY

The software for modelling earthquake sources and performing seismic wave propagation simulation SPECFEM3D is publicly available: <https://geodynamics.org/resources/specfem3dcartesian>. The 1-Hz and 30 sec sampling rate RINEX GNSS data for the M_w 6.2 Suzu earthquake was obtained from <https://www.terasat.co.jp>. IONEX data was obtained from NASA's Archive of Space Geodesy Data CDDIS <https://cddis.nasa.gov/>.

REFERENCES

- Afraimovich, E.L., Astafieva, E.I. & Kirushkin, V.V., 2006. Localization of the source of ionospheric disturbance generated during an earthquake, *Int. J. Geomagnet. Aeron.*, **6**, doi:10.1029/2004GI000092.
- Afraimovich, E.L., Astafyeva, E., Demyanov, V.V., Edemskiy, I., Gavrilyuk, N.S., Ishin, A. & Kosogorov, E.A., 2013. A review of GPS/GLONASS studies of the ionospheric response to natural and anthropogenic processes and phenomena, *J. Space Weather Space Clim.*, **3**, doi:10.1051/SWSC/2013049.
- Ampuero, J.P., 2002. Etude physique et numérique de la nucléation des séismes, *PhD thesis*, University of Paris VII, France.
- Astafyeva, E. & Heki, K., 2009. Dependence of waveform of near-field coseismic ionospheric disturbances on focal mechanisms, *Earth, Planets Space*, **61**, doi:10.1186/BF03353206.

- Astafeyeva, E., Rolland, L.M. & Sladen, A., 2014. Strike-slip earthquakes can also be detected in the ionosphere, *Earth planet. Sci. Lett.*, **405**, doi:10.1016/j.epsl.2014.08.024.
- Astafeyeva, E., Shalimov, S., Olshanskaya, E. & Lognonné, P.H., 2013. Ionospheric response to earthquakes of different magnitudes: larger quakes perturb the ionosphere stronger and longer, *Geophys. Res. Lett.*, **40**, doi:10.1002/GRL.50398.
- Astafeyeva, E. & Shults, K., 2019. Ionospheric GNSS imagery of seismic source: possibilities, difficulties, and challenges, *J. geophys. Res.*, **124**, doi:10.1029/2018JA026107.
- Bagiya, M.S., Heki, K. & Gahalaut, V.K., 2023. Anisotropy of the near-field coseismic ionospheric perturbation amplitudes reflecting the source process: the 2023 February Turkey earthquakes, *Geophys. Res. Lett.*, **50**, doi:10.1029/2023GL103931.
- Bravo, M., Benavente, R., Foppiano, A., Urra, B. & Ovalle, E., 2022. Traveling ionospheric disturbances observed over South-America after lithospheric events: 2010–2020, *J. geophys. Res.*, **127**, doi:10.1029/2021ja030060.
- Brissaud, Q. & Astafeyeva, E., 2020. Near-real-time detection of co-seismic ionospheric disturbances using machine learning, *J. geophys. Int.*, **230**(3), doi:10.1093/gji/ggac167.
- Cahyadi, M.N., Cahyadi, M.N. & Heki, K., 2015. Coseismic ionospheric disturbance of the large strike-slip earthquakes in North Sumatra in 2012: Mw dependence of the disturbance amplitudes, *J. geophys. Int.*, **200**, doi:10.1093/GJI/GGU343.
- Calais, E. & Minster, J.B., 1998. GPS, earthquakes, the ionosphere, and the space shuttle, *Phys. Earth planet. Inter.*, **105**, doi:10.1016/S0031-9201(97)00089-7.
- Catherine, J.K., Maheshwari, D.U., Gahalaut, V.K., Roy, P.N.S., & Puviarasan, N., 2017. Ionospheric disturbances triggered by the 25 April, 2015 M7.8 Gorkha earthquake, Nepal: constraints from GPS TEC measurements, *J. Asian Earth Sci.*, **133**, doi:10.1016/J.JSEAES.2016.07.014.
- Chai, Y. & Jin, S., 2021. Two-azimuth co-seismic ionospheric disturbances following the 2020 Jamaica earthquake from GPS observations, *J. geophys. Res.*, **126**, doi:10.1029/2020JA028995.
- Choy, G.L. & Boatwright, J.L., 1995. Global patterns of radiated seismic energy and apparent stress, *J. geophys. Res.*, **100**, doi:10.1029/95JB01969.
- Chum, J., Hruska, F., Zednik, J. & Lastovicka, J., 2012. Ionospheric disturbances (infrasound waves) over the Czech Republic excited by the 2011 Tohoku earthquake, *J. geophys. Res.*, **117**, doi:10.1029/2012JA017767.
- Gao, Y. et al., 2023. Acoustic-gravity waves generated by a point source on the ground in a stratified atmosphere-Earth structure, *J. geophys. Int.*, **232**, doi:10.1093/gji/ggac364.
- Harris, R.A., Barall, M., Archuleta, R.J., Dunham, E.M., Aagaard, B.T., Ampuero, J.-P. & Bhat, H.S., 2009. The SCEC/USGS dynamic earthquake rupture code verification exercise, *Seismol. Res. Lett.*, **80**, doi:10.1785/GSSRL.80.1.119.
- Harris, R.A., Barall, M., Aagaard, B.T., Ma, S., Roten, D., Olsen, K.B. & Duan, B., 2018. A suite of exercises for verifying dynamic earthquake rupture codes, *Seismol. Res. Lett.*, **89**, doi:10.1785/0220170222.
- Haskell, N.A., 1964. Total energy and energy spectral density of elastic wave radiation from propagating faults, *Bull. seism. Soc. Am.*, **54**(6A), 1811–1841.
- Heale, C.J., Snively, J.B., Hickey, M.P. & Ali, C.J., 2014. Thermospheric dissipation of upward propagating gravity wave packets, *J. geophys. Res.*, **119**, doi:10.1002/2013JA019387.
- Hines, C.O., 1960. Internal atmospheric gravity waves at ionospheric heights, *Can. J. Phys.*, **38**, doi:10.1139/P60-150.
- Ida, Y., 1972. Cohesive force across the tip of a longitudinal-shear crack and Griffith's specific surface energy, *J. geophys. Res.*, **77**, doi:10.1029/JB077i020p03796.
- Ide, S. & Beroza, G.C., 2001. Does apparent stress vary with earthquake size?, *Geophys. Res. Lett.*, **28**, doi:10.1029/2001GL013106.
- Inchin, P.A., Snively, J.B., Zettergren, M.D., Komjathy, A., Verkhoglyadova, O.P. & Ram, S.T., 2020. Modeling of ionospheric responses to atmospheric acoustic and gravity waves driven by the 2015 Nepal 7.8 Gorkha earthquake, *J. geophys. Res.*, **125**, doi:10.1029/2019JA027200.
- Inchin, P.A., Snively, J.B., Williamson, A., Melgar, D., Guerrero, J.A. & Zettergren, M.D., 2020. Mesopause airglow disturbances driven by non-linear infrasonic acoustic waves generated by large earthquakes, *J. geophys. Res.*, **125**, doi:10.1029/2019JA027628.
- Inchin, P.A., Snively, J., Kaneko, Y., Kaneko, Y., Zettergren, M.D. & Komjathy, A., 2021. Inferring the evolution of a large earthquake from its acoustic impacts on the ionosphere, *AGU Adv.*, **2**, doi:10.1029/2020AV000260.
- Inchin, P.A. et al., 2023. Multi-layer evolution of acoustic-gravity waves and ionospheric disturbances over the United States after the 2022 Hunga Tonga volcano eruption, *AGU Adv.*, **4**, doi:10.1029/2023AV000870.
- IRIS DMC, 2013. Data Services Products: EQEnergy Earthquake energy & rupture duration, doi:10.17611/DP/EQE.1.doi:10.17611/DP/EQE.1.
- Kakinami, Y., Saito, H., Yamamoto, T., Chen, C.-H., Yamamoto, M., Nakajima, K., Liu, J.-Y. & Watanabe, Sh., 2021. Onset altitudes of co-seismic ionospheric disturbances determined by multiple distributions of GNSS TEC after the foreshock of the 2011 Tohoku earthquake on March 9, 2011, *Earth Space Sci.*, **8**, doi:10.1029/2020EA001217.
- Kamogawa, M. et al., 2016. A possible space-based tsunami early warning system using observations of the tsunami ionospheric hole, *Sci. Rep.*, **6**, doi:10.1038/srep37989.
- Kanai, R., Kamogawa, M., Nagao, T., Smith, A. & Guillas, S., 2022. Robust uncertainty quantification of the volume of tsunami ionospheric holes for the 2011 Tohoku-Oki Earthquake: towards low-cost satellite-based tsunami warning systems, *Nat. Haz. Earth Syst. Sci.*, **22**, doi:10.5194/nhess-22-849-2022.
- Kaneko, Y., Lapusta, N. & Ampuero, J.-P., 2008. Spectral element modeling of spontaneous earthquake rupture on rate and state faults: effect of velocity-strengthening friction at shallow depths, *J. geophys. Res.*, **113**, doi:10.1029/2007JB005553.
- Kaneko, Y. & Lapusta, N., 2010. Supershear transition due to a free surface in 3-D simulations of spontaneous dynamic rupture on vertical strike-slip faults, *Tectonophysics*, **493**, doi:10.1016/J.TECTO.2010.06.015.
- Kaneko, Y. & Shearer, P.M., 2014. Seismic source spectra and estimated stress drop derived from cohesive-zone models of circular subshear rupture, *J. geophys. Int.*, **197**, doi:10.1093/gji/ggu030.
- Kaneko, Y. & Goto, H., 2022. The origin of large, long-period near-fault ground velocities during surface-breaking strike-slip earthquakes, *Geophys. Res. Lett.*, **49**, doi:10.1029/2022gl098029.
- Komatitsch, D. & Tromp, J., 1999. Introduction to the spectral element method for three-dimensional seismic wave propagation, *J. geophys. Int.*, **139**, doi:10.1046/J.1365-246X.1999.00967.X.
- Komjathy, A., Yang, Y.-M., Meng, X., Verkhoglyadova, O.P., Mannucci, A.J. & Langley, R.B., 2016. Review and perspectives: understanding natural-hazards-generated ionospheric perturbations using GPS measurements and coupled modeling, *Radio Sci.*, **51**, doi:10.1002/2015RS005910.
- Kostrov, B.V., 1974. Seismic moment and energy of earthquakes and seismic flow of rock, *Izv. Acad. Sci., USSR, Phys. Solid Earth*, **1**, 23–40.
- Maletckii, B. & Astafeyeva, E., 2021. Determining spatio-temporal characteristics of coseismic travelling ionospheric disturbances (CTID) in near real-time, *Sci. Rep.*, **11**, doi:10.1038/S41598-021-99906-5.
- Manta, F., Occhipinti, G., Feng, L. & Hill, E.M., 2020. Rapid identification of tsunamigenic earthquakes using GNSS ionospheric sounding, *Sci. Rep.*, **10**, doi:10.1038/S41598-020-68097-W.
- Martire, L., Krishnamoorthy, A., Vergados, P., Romans, L., Szilágyi, B., Meng, X. & Anderson, J.L., 2022. The GUARDIAN system—a GNSS superlateral real-time disaster information and alert network, *GPS Solut.*, **27**, doi:10.1007/s10291-022-01365-6.
- Maruyama, T., Shinagawa, H., Yusupov, K. & Akchurin, A., 2017. Sensitivity of ionosonde detection of atmospheric disturbances induced by seismic Rayleigh waves at different latitudes, *Earth, Planets Space*, **69**, doi:10.1186/S40623-017-0600-Z.
- Meng, X., Ravanelli, M., Komjathy, A. & Verkhoglyadova, O.P., 2022. On the north-south asymmetry of co-seismic ionospheric disturbances during the 16 September 2015 Illapel M8.3 earthquake, *Geophys. Res. Lett.*, **49**, doi:10.1029/2022gl098090.

- Obenberger, K.S., Bowman, D. C. & Dao, E., 2022. Identification of acoustic wave signatures in the ionosphere from conventional surface explosions using MF/HF Doppler sounding, *Radio Sci.*, **57**, doi:10.1029/2021RS007413.
- Palmer, A.C. & Rice, J.R., 1973. The growth of slip surfaces in the progressive failure of over-consolidated clay, *Proc. R. Soc. Lond.*, **332**, doi:10.1029/JB077i020p03796.
- Sevalova, N.P., Sankov, V.A., Astafyeva, E. & Zhupityaeva, A.S., 2014. Threshold magnitude for Ionospheric TEC response to earthquakes, *J. Atmos. Solar-Terrest. Phys.*, **108**, doi:10.1016/J.JASTP.2013.12.014.
- Picone, J.M., Hedin, A.E., Drob, D.P. & Aikin, A.C., 2002. NRLMSISE-00 empirical model of the atmosphere: statistical comparisons and scientific issues, *J. geophys. Res.*, **107**, doi:10.1029/2002JA009430.
- Press, F. & Harkrider, D.G., 1962. Propagation of acoustic-gravity waves in the atmosphere, *J. geophys. Res.*, **67**, doi:10.1029/JZ067I010P03889.
- Rivera, L. & Kanamori, H., 1964. Representations of the radiated energy in earthquakes, *J. geophys. Int.*, **162**, doi:10.1111/j.1365-246X.2005.02648.x.
- Sabatini, R., Bailly, C., Marsden, O., Marsden, O. & Gainville, O., 2016. Characterization of absorption and non-linear effects in infrasound propagation using an augmented Burgers' equation, *J. geophys. Int.*, **207**, doi:10.1093/GJI/GGW350.
- Sanchez, S.A., Kherani, E.A., Astafyeva, E. & de Paula, E.R., 2022. Ionospheric disturbances observed following the ridgecrest earthquake of 4 July 2019 in California, USA, *Remote Sensing*, **14**, doi:10.3390/rs14010188.
- Scholz, C.H., Aviles, C.A. & Wesnousky, S.G., 1986. Scaling differences between large interplate and intraplate earthquakes, *Bull. seism. Soc. Am.*, **76**(1), 65–70.
- Snively, J.B., 2013. Mesospheric hydroxyl airglow signatures of acoustic and gravity waves generated by transient tropospheric forcing, *Geophys. Res. Lett.*, **40**, doi:10.1002/GRL.50886.
- Sunil, A.S., Bagiya, M.S., Bletery, Q. & Ramesh, D.S., 2021. Association of ionospheric signatures to various tectonic parameters during moderate to large magnitude earthquakes: case study, *J. geophys. Res.*, **126**, doi:10.1029/2020JA028709.
- Sutherland, L.C. & Bass, H.E., 2004. Atmospheric absorption in the atmosphere up to 160 km, *J. acoust. Soc. Am.*, **115**, doi:10.1121/1.1631937.
- Schwartz, S.Y. & Rokosky, J.M., 2007. Slow slip events and seismic tremor at circum-Pacific subduction zones, *Rev. Geophys.*, **45**, doi:10.1029/2006RG000208.
- Zedek, F., Rolland, L., Mikesell, T.D., Sladen, A., Delouis, B., Twardzik, C. & Coïsson, P., 2021. Locating surface deformation induced by earthquakes using GPS, GLONASS and Galileo ionospheric sounding from a single station, *Adv. Space Res.*, **68**, doi:10.1016/J.ASR.2021.06.011.
- Zettergren, M.D. & Snively, J.B., 2015. Ionospheric response to infrasonic-acoustic waves generated by natural hazard events, *J. geophys. Res.*, **120**, doi:10.1002/2015JA021116.
- Zettergren, M.D. & Snively, J.B., 2019. Latitude and longitude dependence of ionospheric TEC and magnetic perturbations from infrasonic-

acoustic waves generated by strong seismic events, *Geophys. Res. Lett.*, **46**, doi:10.1029/2018GL081569.

APPENDIX: THE RESULTS OF 2-D SUPPLEMENTAL SIMULATIONS

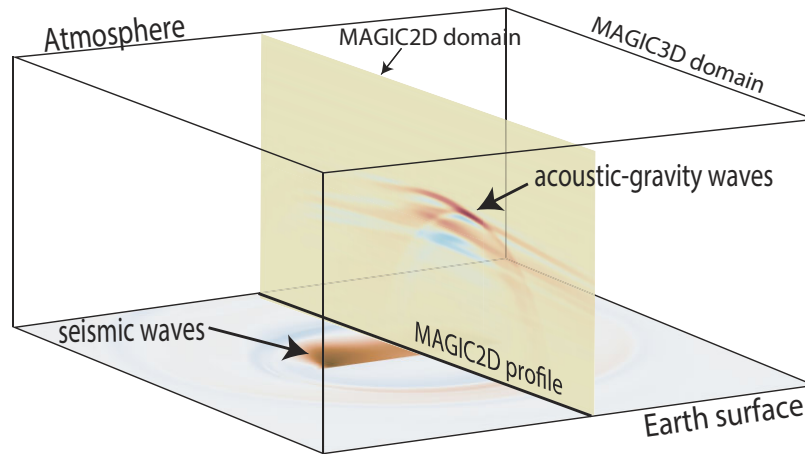
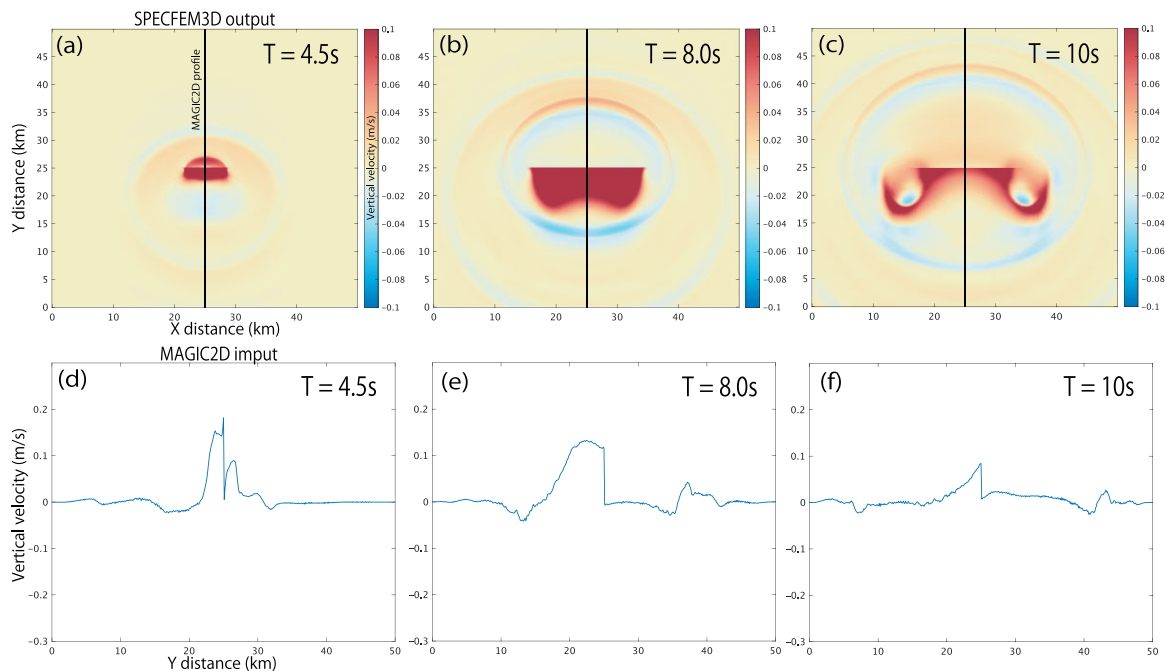
Due to limitation in computational resources, it was unfeasible to perform comprehensive investigations within a 3-D atmospheric numerical model across all possible earthquake source parameter variations. Instead, we pursued a strategy involving 2-D atmospheric simulations as an initial exploration to identify the key earthquake source parameters influencing AW generation and propagation to the upper atmosphere. In the 2-D simulations, we used a 1-D temporally and spatially varying seismic wave source (vertical velocities at the surface) as the lower boundary condition for the atmospheric model, generating AWs within a planar Cartesian domain (Fig. A1). The simulations spanned 8 distinct earthquake models characterized by variations in fault size, fault depth, magnitude (M_w) and stress drop. All of these models entailed bilateral rupture in reverse fault configurations, as detailed in Table A1. The choice of the slice for 2-D atmospheric simulation from 3-D seismic wave propagation simulation is demonstrated in Fig. A2 at 3 moments of time.

We note that a comprehensive view of the disparities between 3-D and 2-D simulations is presented in Fig. A4. The difference is particularly evident as AWs propagate to higher altitudes. We find it is feasible to perform these simulations and compare results, but only with 2-D versus 2-D. After obtaining some insight on source parameter impacts on AW generation and propagation from 2-D simulations, we moved to 3-D atmospheric model simulations and those results are presented in the main text of the paper.

Supplementing the analysis of correlations discussed in the main text, here we provide additional ones based on 2-D atmospheric model simulations. Our analysis centred on comparing earthquake source parameters and the maximum absolute vertical fluid velocity amplitudes at an altitude of 250 km, where AWs are commonly detected with GNSS TEC observations. Several noteworthy trends emerged from this comparison: (1) with the exception of Simulation #S2, which deviated in terms of earthquake magnitude, a fairly linear correlation materialized between stress drop and AW amplitudes (Fig. A3a), (2) even Simulation #S2 exhibited alignment with a linear trend when contrasted with radiated energy (Fig. A3b) and (3) metrics such as maximum uplift, maximum velocity, fault dimension and fault depth exhibited weaker correlations with AW amplitudes in comparison with stress drop or radiated energy.

Table A1. Additional earthquake source models used for 2-D atmospheric simulations.

Sim #	Faulting type/rupture type	Fault size ($L_x \times L_y$)/depth	M_w /stress drop	Radiated energy
S1	Thrust/bilateral	$20 \times 10/0$ km	6.5/4.3 MPa	10.4×10^{13} J
S2	Thrust/bilateral	$12 \times 6/0$ km	6.0/4.2 MPa	2.0×10^{13} J
S3	Thrust/bilateral	$16 \times 8/0$ km	6.5/8.5 MPa	34.6×10^{13} J
S4	Thrust/bilateral	$29 \times 14.5/0$ km	6.5/1.2 MPa	4.6×10^{13} J
S5	Thrust/bilateral	$32 \times 16/1$ km	6.5/1.6 MPa	5.8×10^{13} J
S6	Thrust/bilateral	$19 \times 9/1$ km	6.5/8.5 MPa	31.9×10^{13} J
S7	Thrust/bilateral	$32 \times 16/8$ km	6.5/.5 MPa	4.8×10^{13} J
S8	Thrust/bilateral	$19.5 \times 9.5/10.1$ km	6.5/8.4 MPa	29.0×10^{13} J

**Figure A1.** Earthquake-atmosphere simulation configuration. Dynamically exited seismic waves at the surface from 3-D seismic wave propagation simulations (vertical component) are used as a bottom boundary condition for 2-D atmospheric model.**Figure A2.** (a–f) Seismic wave dynamics (vertical component) at the surface at 3 moments of time from Simulation #S1. Black solid lines panels (a)–(c) indicate slices used for 2-D atmospheric simulations. Panels (d)–(f) illustrate surface vertical velocity along chosen slices.

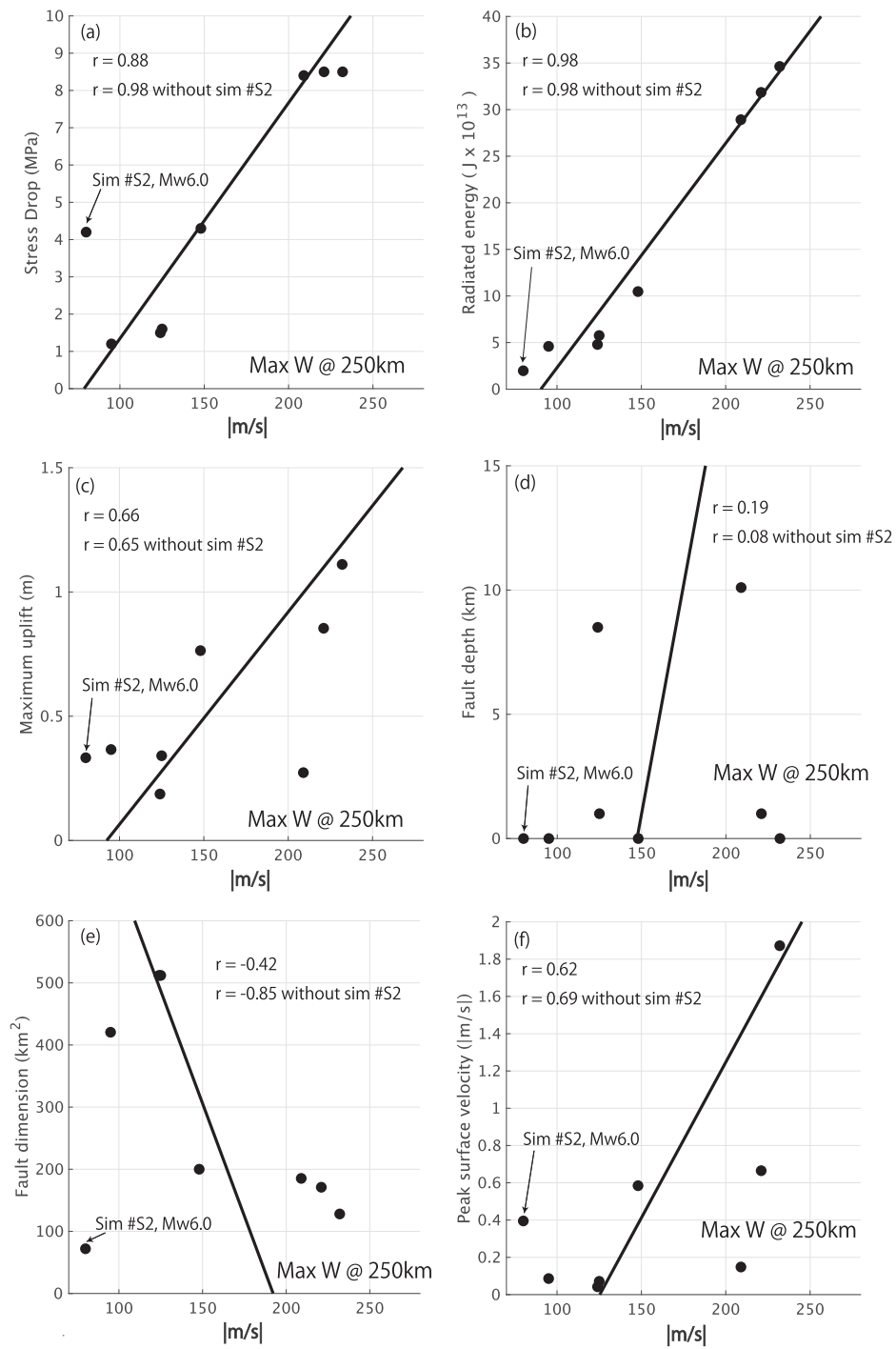


Figure A3. Correlations between maximum absolute vertical fluid velocity amplitudes at 250 km altitude and (a) stress drop on fault, (b) radiated energy, (c) maximum uplift along chosen slice, (d) fault depth, (e) fault size and (f) maximum velocity along chosen slice.

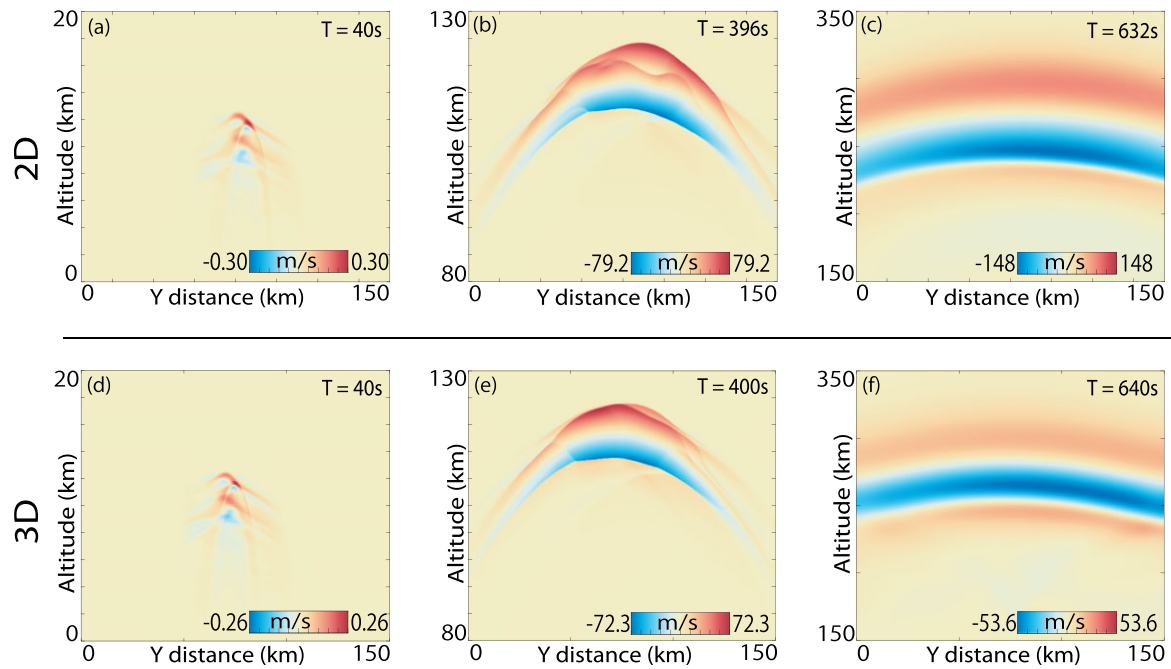


Figure A4. (a–c) AW dynamics (corresponding vertical fluid velocities) in the upper atmosphere at 3 moments of time from 2-D and (d–f) 3-D simulations with earthquake source #S1 as specified in the Table A1.